Depletion and refertilisation of the lithospheric mantle below the Kapsiki plateau (Northern Cameroon Volcanic Line) deduced from trace element and H_2O systematics in mantle xenoliths

Siggy S. Nformidah-Ndah [a,*], Peter M.E. Tollan [a,b], Joerg Hermann [a], Jean Pierre Tchouankoue [c]

[a] *Institut für Geologie, Universität Bern, Baltzerstrasse 1+3, 3012, Bern, Switzerland*
[b] *Institut für Geochemie und Petrologie, ETH Zürich, NW Clausiusstrasse 25, 8092, Zurich, Switzerland*
[c] *Department of Earth Sciences, University of Yaounde I, P.O. Box 812, Yaounde, Cameroon*

ARTICLE INFO

ABSTRACT

Clinopyroxene bearing spinel harzburgites recovered from Cenozoic alkaline basalts from the Kapsiki plateau were investigated with the aim of understanding depletion and enrichment processes in the subcontinental mantle below a major tectonic line. Concentrations of major and trace elements (including H) were determined in-situ in olivine, orthopyroxene, clinopyroxene and spinel by EPMA, LA-ICP-MS and FTIR. The xenoliths are refractory with high olivine (0.91–0.92) and orthopyroxene (0.92–0.93) Mg# coupled with relatively high modal proportions of clinopyroxene (5–8%) and a remarkably wide range in clinopyroxene Mg# (0.91–0.94), interpreted to reflect high degrees of partial melting followed by modal and chemical metasomatic refertilization. A fractional partial melting model of orthopyroxene trace elements in a depleted mantle indicates 20–30% of melting. Clinopyroxenes show two groups based on their CaO contents (18.7–18.9 and 20.6–22.6 wt %) suggesting a secondary origin and modal metasomatism. The low Ca clinopyroxenes were the latest to be formed, and the wide range of clinopyroxene Mg# shows a lack of equilibrium with the coexisting minerals. The high Ca clinopyroxenes record ancient metasomatic events that are also documented in orthopyroxene. Cryptic metasomatism is shown by strong progressive enrichments in LREEs and MREEs of orthopyroxene and clinopyroxene. Th vs La and Sr vs Nd of clinopyroxene are used to identify different generations of metasomatism. Ti/Eu vs (La/Yb)$_N$ and Zr/Hf systematics indicate that the metasomatising agent has both a carbonatite and a silicate component. The structural hydroxyl contents of the different mineral phases are very low (<1 ppm for olivine, 40–48 ppm for orthopyroxene and 164–277 ppm for clinopyroxene). The very low water contents compared to typical sub-continental peridotites could be attributed to the depleted nature of the xenoliths or reflect lower water activities of carbonatitic melts relative to alkaline melts. Estimated fO_2 values expressed as ΔlogFMQ, (where FMQ corresponds to the fayalite magnetite-quartz oxygen buffer) range from -0.42 to -0.26 and are consistent with minor OH stretching regions of 3520 cm^{-1} in orthopyroxene, related to a ferric iron defect.

The combination of textural investigations, major, and trace element and H_2O data suggests that a refractory subcontinental mantle was affected by several episodes of intraplate metasomatism dominated by silicate-carbonatite melts above the North-Eastern end of the Cameroon Volcanic Line.

1. Introduction

The subcontinental lithospheric mantle documents a long and complex evolution history with multiple depletion and enrichment events (Griffin et al., 2008). Disentangling the sequences of events and distinguishing between modal and cryptic metasomatism is often challenging. With the development of in-situ trace element analyses with low detection limits, the systematic study of major and trace compositions of clinopyroxene has been instrumental to constrain different types of metasomatic agents (e.g. Coltorti et al., 1999; Uenver-Thiele et al., 2017). Classifications traditionally focused on clinopyroxene compositions, as it is the phase in peridotites with the highest concentration of incompatible elements (Eggins et al., 1998; Witt-Eickschen and O'Neill, 2005). For example discrimination diagrams using Ti/Eu coupled with

La/Yb (Coltorti et al., 1999) or Zr/Hf (Uenver Thiele et al., 2017) in clinopyroxene have been used to distinguish between carbonatite melts, carbonatite-silicate melts, silicate melts or subduction-related fluids as metasomatic agents. Hydrogen is an additional incompatible element in olivine, orthopyroxene and clinopyroxene (Hirschmann et al., 2009) that can give important insights into equilibrium and refertilization processes since H_2O is a major component in many of these reacting fluids/melts (Peslier et al., 2012; Doucet et al., 2014; Tollan et al., 2015). Combined investigations of H together with incompatible trace elements in ortho- and clinopyroxene in mantle peridotites are a powerful tool to investigate complex mantle metasomatism (Peslier et al., 2012).

The Cameroon Volcanic Line (CVL) provides a good opportunity to investigate the sub-continental lithospheric mantle in a complex fault zone, as many alkaline basalts that carry mantle xenoliths have been found (Pintér et al., 2015; Tamen et al., 2015; Ngounouno et al., 2008; Caldeira and Munhá, 2002; Lee et al., 1996). The N30°E trending CVL formed during the Cenozoic and is segmented by several N70°E shear zones of Pan-African age, which cut across both the continental crust and the upper mantle to depths of 160 km (Déruelle et al., 2007). The Pan African belt was formed by the convergence and collision of the San Francisco-Congo cratons, the West African craton and a Pan African mobile domain (Toteu et al., 2004; Tokam et al., 2010). In such orogenic environments where more than one crustal block has been involved, geodynamic processes such as subduction, collision or lithospheric delamination can lead to the destruction of the base of the lithosphere and hence significant local modifications of the upper mantle (Liu et al., 2016).

The Kapsiki plateau volcanism of Oligocene age (32-29 Ma, Dunlop, 1983) is close to that of the oldest volcanic rocks (rhyolites, 64.4 ± 0.4 Ma) of the CVL evidenced in the southern part of Chad at about 300 km to the NNE, reported by Mbowou et al. (2012). The Kapsiki plateau bears the northernmost known occurrence of mantle xenoliths along the CVL (Tamen et al., 2015) providing an important endmember to investigate depletion and metasomatic processes in the lithospheric mantle. Extended volcanism during the Cenozoic (Déruelle et al., 2007), interactions between magmas of sub-lithospheric origin and the SCLM and the speculated juvenile state of the lithospheric mantle (Marzoli et al., 2000, 2015) represent processes that might have led to such metasomatism. An added advantage is that some of the Kapsiki xenoliths are highly depleted (this work), therefore, they can easily record minor metasomatic events and are instrumental in providing insights into the state of the mantle before interactions with percolating melts, which can quickly conceal earlier metasomatic events. The Kapsiki xenoliths, therefore, are a key to understand and decipher the SCLM below the rest of the line. This work presents new data on mineral major and trace elements plus H_2O contents of mantle xenoliths brought to the surface by Cenozoic alkaline magmas from the Kapsiki plateau in the Kila area and discusses their implication for the nature and evolution of the SCLM below an important lithospheric fault zone. A combination of data from different analytical techniques is used to decode the different mantle processes like partial melting, metasomatism and the different possible metasomatic agents, which modified the mantle and are still debated for the CVL (Pintér et al., 2015; Tamen et al., 2015). New clinopyroxene trace element discrimination diagrams for inferring small degrees of metasomatism by silicate-carbonatite melts are developed and have the potential to be applied to cryptic metasomatism documented in orthopyroxene.

2. Geological setting

The Kapsiki plateau is located in the Far-Northern part of Cameroon (Fig. 1). This Far-Northern part is composed of three main geological units: quaternary deposits of Lake Chad and the surrounding areas, (Adjia et al., 2013; Tsozué et al., 2017), volcanic to sub-volcanic complexes associated with the Cameroon Volcanic Line (CVL) (Ngounouno

et al., 2000; Déruelle et al., 2001, 2007) and igneous and metamorphic rocks related to the Cameroon Pan African Belt (Toteu et al., 2001).

The Kapsiki plateau straddles the Cameroon-Nigeria boundary and is the northernmost known volcanic zone of the CVL (Ngounouno et al., 2008; Tamen et al., 2015). The CVL (Fig. 1a) is the only intraplate alkaline to transitional (Moundi et al., 1996, 2007) volcanic province comprising of a continental and an oceanic sector, which stretches from the Atlantic Islands of Pagalu through the Gulf of Guinea into the African continent. It is a Y-Shaped lineament composed of Tertiary to Holocene volcanoes (Fitton, 1983) built on crustal weaknesses on a distance of up to 1600 km.

The Kapsiki plateau culminates at mean altitudes of 800 m, it is dominated by volcanic complexes and covers an area of 150 km^2 (Fig. 1b). Volcanic activity in the Kapsiki plateau is distinguished from other CVL volcanoes by a relative abundance of felsic and intermediate rocks relative to basanites. Felsic and intermediate volcanism was accompanied by abundant intrusive rocks not reported in other parts of the CVL. In terms of age, felsic, transitional and mafic volcanic rocks are relatively old and are of similar ages, which can be bracketed between 27 and 35 Ma (Vincent and Armstrong, 1973; Dunlop, 1983). The alignment of volcanic plugs corresponds to major directions N30°E that is dominant and subsidiary N65°E and N165°E. The three directions correspond to the direction of the Cameroon Line, the Adamawa Shear Zone and the Benue trough, which are main regional trends, well known in the Precambrian basement (Regnoult, 1986). The orientation of these three main regional lineaments in conjunction with coeval ages of felsic, intermediate and mafic volcanism (27 and 35 Ma) suggests that a single reactivation episode in the Tertiary led to the volcanic activity in the Kapsiki plateau. Moreover, volcanic ages for the Kapsiki plateau basalts contribute to rule out any polarity of ages along the CVL, in response to the displacement of the African plate towards the Northeast.

Mantle xenoliths were sampled in Cenozoic alkaline basaltic flow around Longitude 13°36′E and latitude 10°26′N (Fig. 1b) at about 5 km to the south-west of Kila village. The xenoliths are sub-circular in shape and are generally less than 20 cm in diameter. Mantle xenoliths are hosted by a basaltic flow, which is a south-western branch of a SE-NW oriented flow that also extend from Rhumsiki to Liri.

From a geodynamic point of view, the Kapsiki plateau lies above a Pan-African basement, which belongs to the northern unit of the Pan-African domain of Cameroon. The lithology comprises sensu-stricto Pan-African granitoids and their host orthogneissic basement. The oldest Nd and Hf TDM ages recorded in the area are Paleoproterozoic (Bute et al., 2019), which differ from Pan-African rocks with Archean heritage found elsewhere in Pan-African terrains such in the Adamawa-Yade domain (Ganwa et al., 2016). The Kapsiki plateau is located at the southern edge of the Saharan Metacraton (GoussiNgalamo et al., 2018, Fig. 1B) and the geodynamic model proposed for the Pan-African basement of the Kapsikis is a lithospheric delamination that led to abundant widespread magmatism at about 580 Ma (Bute et al., 2019). Various studies in the field of geodynamics (Ferré et al., 2002) and geophysics (Pasyanos and Nyblade, 2007) point out a lithospheric thinning because in the framework of the delamination model, the decompressional melting of the asthenosphere leads to a diapirism since the mantle removed is to be replaced. The Moho below the Kapsikis is estimated between 24 and 33 km (Poudjom Djomani et al., 1995; Tokam et al., 2010; Kemgang et al., 2020).

3. Analytical methods

Three alteration-free peridotite xenoliths were selected for this study (Ka1, Ka2 and Ka7) after a preliminary study of a large data set done on grain mounts of xenolith mineral phases from peridotites of the CVL. The xenoliths studied were selected as they show a particular huge chemical variation. The xenoliths were cut into glass-mounted polished thin sections (30 μm thick) and demountable, double-polished thick sections (300 μm thick). All subsequent analyses were carried out at the Institute
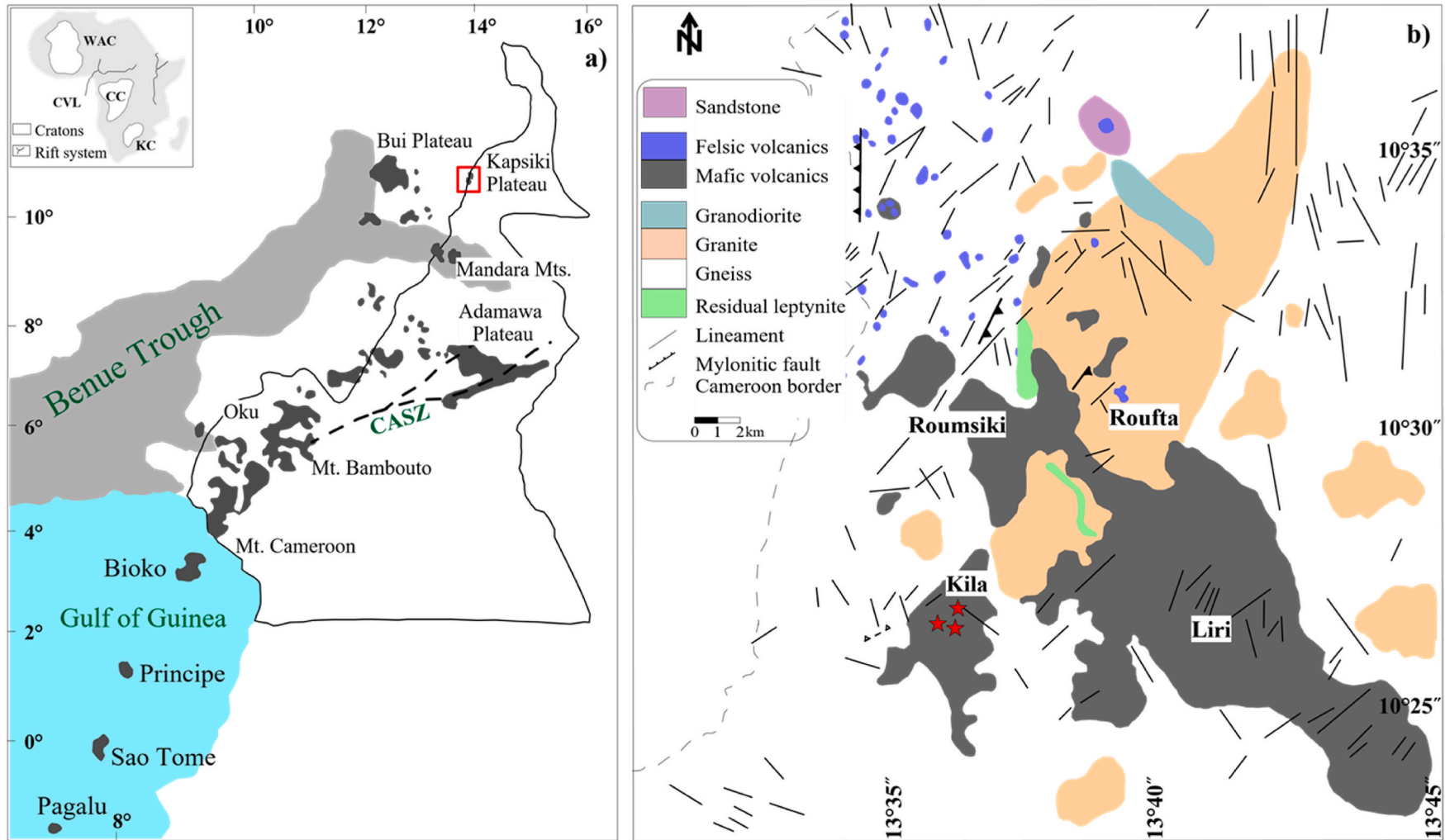
Fig. 1. a: Cameroon Volcanic Line (CVL) with major Cenozoic centers and the Central African Shear Zone (CASZ). The left insert shows the position of the CVL in Africa and the major cratons. b) Geological map of Kapsiki (modified from Tamen et al., 2015) extrapolated from Fig. 1a. The red stars indicate where the xenoliths were collected. (For interpretation of the references to colour in this figure legend, the reader is referred to the Web version of this article.)

of Geological Sciences, University of Bern.

3.1. Electron probe micro-analyser (EPMA)

Major and minor element concentrations of olivine, orthopyroxene, clinopyroxene and spinel were determined using a JEOL JXA 8200 super probe. Data were collected at 15 kV accelerating voltage, 20 nA beam current with a beam diameter of 1–3 μm depending on the size of the grain analyzed. Counting times of 20–60 s were applied depending on the element and mineral analyzed. Natural and synthetic minerals were used as standards. The following elements were analyzed: Si, Ti, Al, Cr, Fe, Mn, Mg, Ni, Ca, Na, K. Where possible, core and rim compositions were measured for olivine and pyroxenes.

3.2. Laser ablation inductively coupled plasma mass spectrometry (LA-ICP-MS)

Trace element concentrations were determined using an Australian Scientific Instrument (now Applied Spectra) Resonetics RESOlutionSE 193 nm excimer laser system with a fast washout two-volume cell, coupled to an Agilent 7900 quadrupole ICP-MS. Ablation was conducted in a He atmosphere at a frequency of 5–10 Hz, energy density of 6 J/cm^2 and a beam diameter of 50–100 μm. The ablated material was extracted in a steam of He (0.4 l/min), which was subsequently combined with Ar (0.88 l/min) and N_2 (3 ml/min) before entering the ICP. The glass NIST 612 was used as the primary standard, with glasses T1G, BHVO and GOR132 as secondary standards (Jochum et al., 2005, 2006, 2011). The elements analyzed were ^{7}Li, ^{23}Na, ^{25}Mg, ^{27}Al, ^{29}Si, ^{31}P, ^{43}Ca, ^{45}Sc, ^{47}Ti, ^{51}V, ^{53}Cr, ^{55}Mn, ^{57}Fe, ^{59}Co, ^{61}Ni, ^{88}Sr, ^{89}Y, ^{90}Zr, ^{93}Nb, ^{178}Hf, ^{208}Pb, ^{232}Th, ^{238}U and the REEs. For olivine, the list was modified due to the substantially lower concentrations of most elements; only ^{7}Li, ^{11}B, ^{23}Na, ^{25}Mg, ^{27}Al, ^{29}Si, ^{31}P, ^{43}Ca, ^{45}Sc, ^{47}Ti, ^{51}V, ^{53}Cr, ^{55}Mn, ^{57}Fe, ^{59}Co, ^{61}Ni, ^{66}Zn, ^{89}Y and ^{90}Zr were measured. The data obtained were evaluated using IOLITE (Paton et al., 2011). The results were normalized using Si (Ka1) and Ca (Ka2 and Ka7) values for clinopyroxene. The choice of Si values for sample Ka1 was because of its variability in Ca contents. For olivine and orthopyroxene, Si values obtained from electron microprobe analysis were used.

3.3. Fourier transform infrared spectroscopy (FTIR)

The H_2O contents of olivine and pyroxenes and information on the local bonding environment of hydrogen were determined by transmission FTIR spectroscopy using a Bruker Tensor II Fourier transform infrared spectrometer equipped with a nitrogen-cooled mercury cadmium telluride (MCT) detector coupled to a Hyperion 3000 microscope with an automated stage. The number of scans was 128; the resolution was set at 4 cm^{-1} with an aperture size of 20 × 20 μm to 50 × 50 μm depending on the grain size and availability of inclusion and lamellae-free zones. The spectra were collected using unpolarised light and on un-oriented crystals. The data obtained were processed using the OPUS software package; the spectra were corrected for atmospheric contamination using the software algorithm before the baseline was subtracted using the concave rubber band correction method using two iterations. The hydrogen contents were calculated using the modified Beer-Lambert Law: $C = A/(I \times t)$, where C is the H_2O concentration (weight ppm), A is the integral area (cm^{-2}) of absorption bands in the region of interest, and I is the integral specific absorption coefficient of minerals (ppm^{-1} cm^{-2}), and t is the thickness of the section (cm). The integrated area was multiplied by 3 to get the total absorbance (Kovacs et al., 2008) and integral specific coefficients of 5.32, 14.84 and 7.09 ppm^{-1}cm^{-2} were used for olivine, orthopyroxene and clinopyroxene respectively (Bell et al., 1995; Bell et al., 2003). Clinopyroxene spectra showing OH bands attributed to the presence of amphibole were excluded during the quantification of the water contents.

4. Results

4.1. Petrography

The Kapsiki xenoliths hosted in Cenozoic alkali basalts are sub-angular to rounded, ranging from 6 to 10 cm across and show a sharp contact with the host basalt. According to the classification of Mercier and Carter (1975), they are coarse-grained with protogranular to porphyroclastic textures (Fig. 2a and b). Olivine and orthopyroxene range in size from 0.2 to 8 mm where the neoblasts are euhedral and the porphyroclasts are subhedral with strain features presenting as cracks. Kink bands are common in large olivine and orthopyroxene porphyroclasts (Fig. 2b). Clinopyroxene is subhedral, much smaller than the coexisting minerals (ranging in size from 0.2 to 1 mm) and sits in interstitial position between olivine and orthopyroxene, with most of them being closely associated to orthopyroxene (Fig. 2a). A few clinopyroxene grains along the boundary with the host basalt show rims with a distinct spongy texture. These textures are also common in the pristine part of the xenoliths (Fig. 2c). Exsolution lamellae of clinopyroxene are common in the central part of orthopyroxene porphyroclasts (Fig. 2d). Vermicular dark-brown spinel occurs as holly-leaf shapes in interstitial position between olivine and pyroxenes (Fig. 2e).

Modal proportions obtained from visual estimates of olivine (~60–64 vol %), orthopyroxene (~30–34%) and clinopyroxene (~4–6%) and projected on Streckeisen (1976) classification diagram of ultramafic rocks fall close to the lherzolite-harzburgite boundary. Sample Ka7 shows the highest proportion of clinopyroxene (~6%). Spinel occurs in minor proportions (~2%) and no hydrous phases are present except for tiny amphibole lamellae in clinopyroxene.

4.2. Mineral chemistry

EPMA and LA-ICP-MS analyses of the different phases are reported in the Supplementary Data Electronic Appendix A and B.

4.2.1. Major elements

Olivine grains are relatively homogeneous with no major core-rim or porphyroclast-neoblast chemical variations. Sample Ka1 is the most refractory with average Mg# (Mg/(Mg + Fe)) of 0.917 ± 0.001 (Fig. 3a) (Supplementary material, Appendix A). Olivine of sample Ka2 and Ka7 has Mg# of 0.914 ± 0.001 and 0.913 ± 0.001 respectively. Orthopyroxene grains have chemically identical porphyroclasts and neoblasts. Calculated Mg# ranges from 0.92 to 0.93 (Supplementary material, Appendix A, Fig. 3d) and are 0.5% (Ka1), 0.3% (Ka2) and 0.6% (Ka7) higher than the coexisting olivines. The TiO$_2$, CaO and Al$_2$O$_3$ contents are low (0.02–0.09, 0.36–0.75 and 1.32–2.31 wt% respectively) while Cr$_2$O$_3$ contents are relatively high (0.29–0.65 wt%). Unlike olivine and orthopyroxene, clinopyroxene shows considerable intergrain chemical variations in TiO$_2$, Cr$_2$O$_3$, CaO, Na$_2$O and Mg# (Supplementary material, Appendix A), with compositions ranging from Cr-rich diopside to Cr-rich augite (En$_{47.7-48.8}$Fs$_{3.3-5.1}$Wo$_{42.4-48.8}$). Two groups can be distinguished based principally on their CaO contents and Mg# (Fig. 3e and f). The first group has low CaO contents (18.7–18.9 wt%) (Supplementary material, Appendix A) and the lowest Mg# (0.91–0.92) and occurs only in sample Ka1. The second group has high CaO contents (20.62–22.57 wt%) and Mg# which vary more, extending to higher values (0.91–0.94) and is found in all samples. Group 1 clinopyroxenes show higher Al$_2$O$_3$ contents (Fig. 3e) in the range of 3.7–3.8 wt% (Supplementary material, Appendix A), group 2 clinopyroxenes show a wider range of Al$_2$O$_3$ contents with values of 2.9–3.8 wt% with sample Ka1 showing the highest values. Spinels from Kapsiki samples are relatively heterogeneous with Cr$_2$O$_3$ contents of 39.0–44.4, 36.2–38.9 and 35.7–38.3 wt%, Al$_2$O$_3$ contents of 23.9–29.8, 28.8–32.1 and 29.1–31.7 wt%, TiO$_2$ contents of 0.11–0.48, 0.11–0.25 and 0.13–0.25 wt% (Supplementary material, Appendix A) in samples Ka1, Ka2 and Ka7 respectively. Mg# are 0.62–0.68 for Ka1 and 0.64–0.68 for Ka2 and Ka7
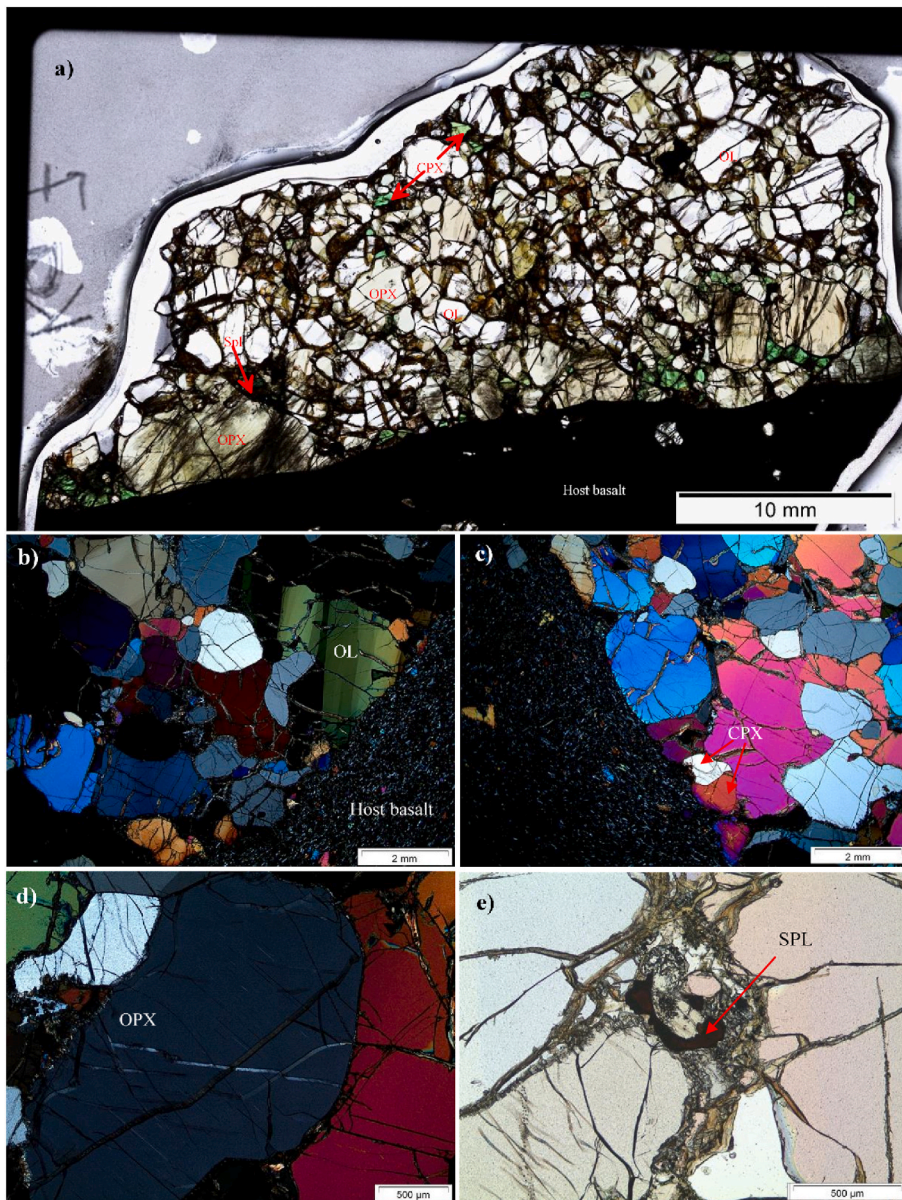
Fig. 2. Thin section scan of Kapsiki xenolith showing large olivine and orthopyroxene crystals, with smaller clinopyroxene in interstitial position (Ka7) (a) and photomicrographs of Kapsiki xenolith; (b) large olivine showing kink bands and a sharp contact at the host basalt-xenolith boundary (Ka1); (c) clinopyroxene which shows no interaction with the host basalt (Ka2); (d) exsolution lamella of clinopyroxene in orthopyroxene (Ka1); (e) dark brown spinel with the coexisting mineral showing melt veinlets (Ka1). (For interpretation of the references to colour in this figure legend, the reader is referred to the Web version of this article.)

while Cr# (Cr/Cr + Al) are 0.47–0.55 for Ka1, 0.43–0.48 for Ka2 and 0.43–0.47 for Ka7. $Fe^{3+}/\Sigma Fe$, with Fe^{3+} calculated based on charge balance, ranges from 0.07 to 0.16 for Ka1 and 0.08–0.19 for Ka2 and Ka7.

4.2.2. Trace elements

Measurements were done in the cores of olivine, orthopyroxene and clinopyroxene. Compared to the global distribution of mantle olivine compositions (De Hoog et al., 2010), Kapsiki olivine contains typical concentrations of Na (46–62 µg/g) and relatively low Al (60–92 µg/g), Ti (5–13 µg/g) and Cr (77–150 µg/g) (Supplementary material, Appendix B). The concentrations of Na, Al, and Cr are correlated, indicating coupled substitutions of the type $CrAlMg_{-1}Si_{-1}$ and $CrNaMg_{-2}$. Lithium correlates with Na in Ka2 and Ka7 at higher Li concentrations, while no correlation is visible in Ka1 that has lower Li contents. Generally, Ka2 and Ka7 olivines plot on a continuous trend whereas Ka1 is situated in a different field (Fig. 4a and b). Calcium (480–610 µg/g) is higher than typical spinel peridotite xenoliths (De Hoog et al., 2010). Although Y (920 ng/g) and Zr (9–13 ng/g) concentrations are very low, a clear distinction between Ka1 and Ka2, Ka7 still exists.

Trace element concentrations of pyroxenes were normalized to the primitive mantle (PM) values of Palme and O'Neill, 2014) (Fig. 5 and 6). Clinopyroxenes from Ka2 and Ka7 (Fig. 5d, f) have minimal inter-grain variation in MREE and HREE concentrations ($(Nd/Yb)_N = 1–3$, $Yb_N = 0.65–1.03$) but significant variation in LREE concentrations ($(La/Yb)_N = 2–23$ and $(La/Nd)_N = 1–9$). Clinopyroxenes from sample Ka1 differ in that they show greater inter-grain variation in MREEs and HREEs in addition to LREEs. PM-normalized trace element plots show strong but variable relative depletions in Rb, Ba, Nb and weak negative Pb and Ti anomalies in samples Ka2 and Ka7 (Fig. 6b). Clinopyroxenes from Ka1 have similar features to those from samples Ka2 and Ka7, but they are more enriched in most elements and show significant intergrain variability. Three groups of TE patterns can be distinguished which are however unrelated to the textures in the sample. Orthopyroxene REEs (Fig. 5a, c, e) generally show a spoon shape with $(Nd/Lu)_N < 1$ and $(La/Nd)_N > 1$. Orthopyroxene from Ka1 shows stronger enrichments in both LREE and MREE, resulting in a flatter overall REE pattern, compared to those of the other samples. Orthopyroxene from Ka7 shows two distinct patterns: a more LREE- and MREE enriched pattern, similar to Ka1, and a second, which is similar to Ka2. Trace element patterns
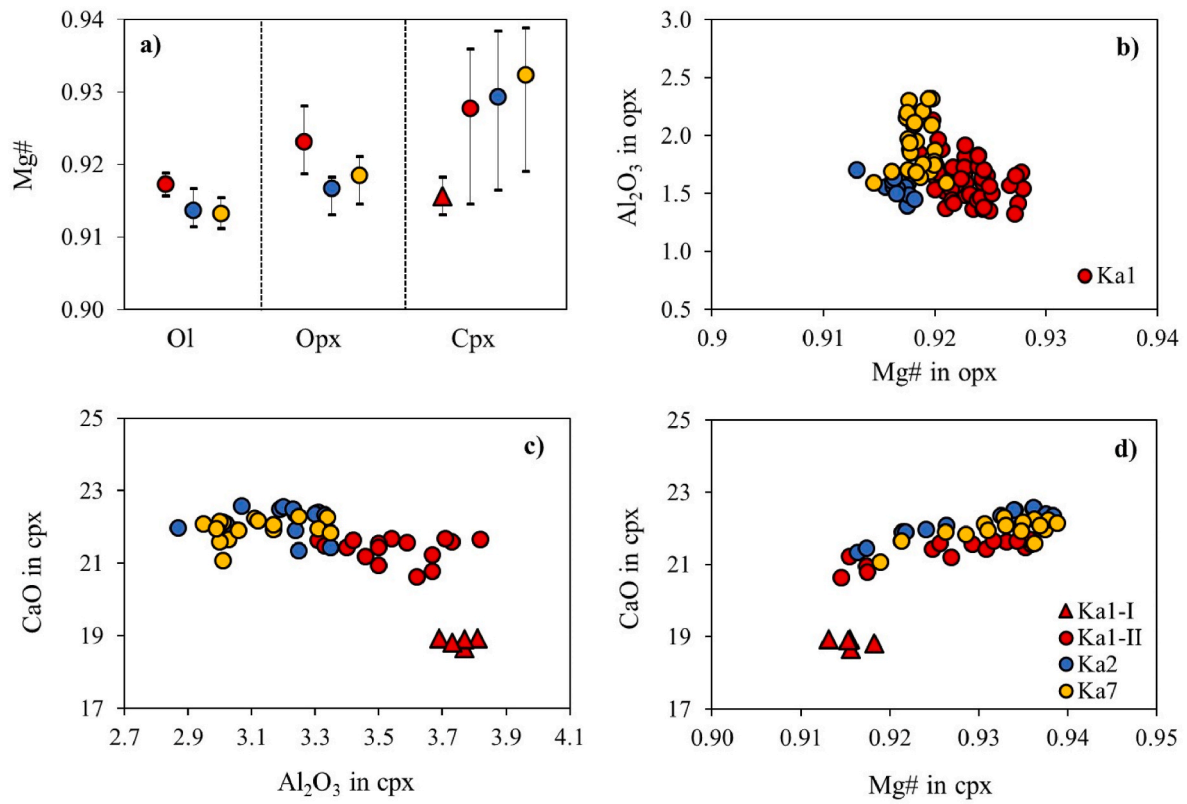
Fig. 3. a: Average Mg# of olivine, ortho- and clinopyroxene. The bars represent minimum and maximum values. b) Major element compositions of orthopyroxene and c) clinopyroxenes showing two generations.
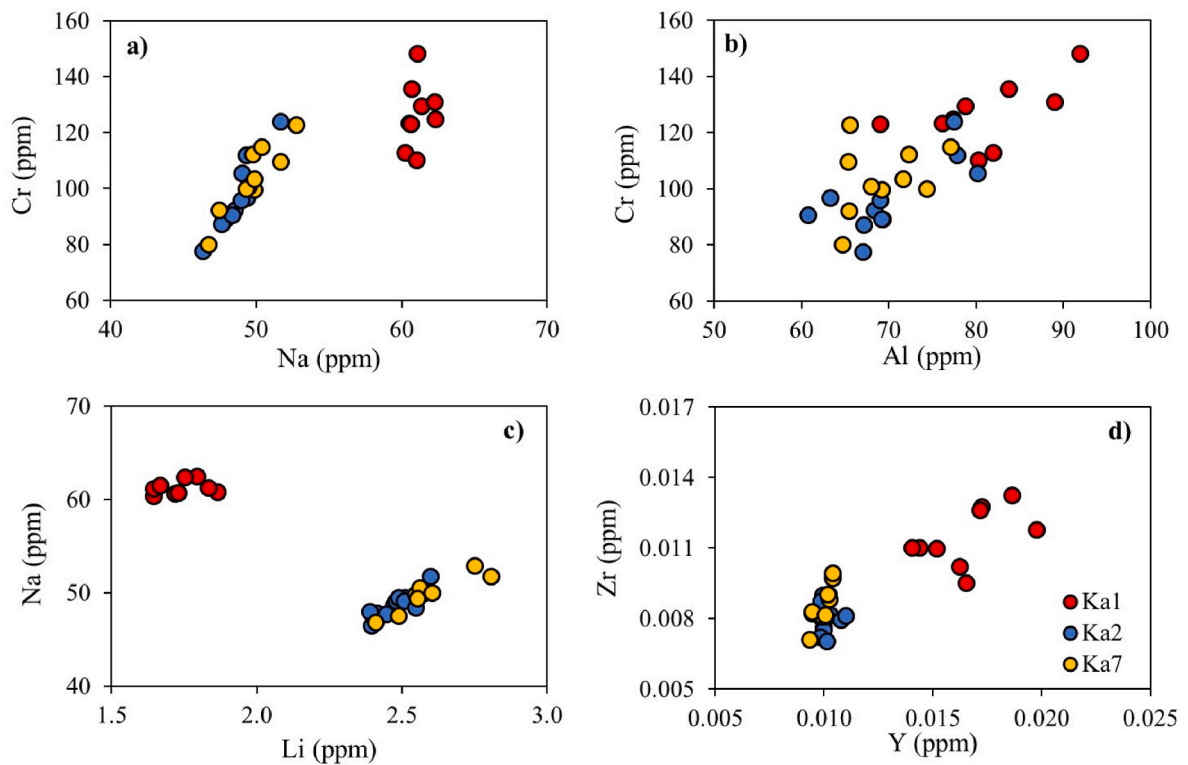

Fig. 4. Trace element compositions of olivines showing two groups of compositions.
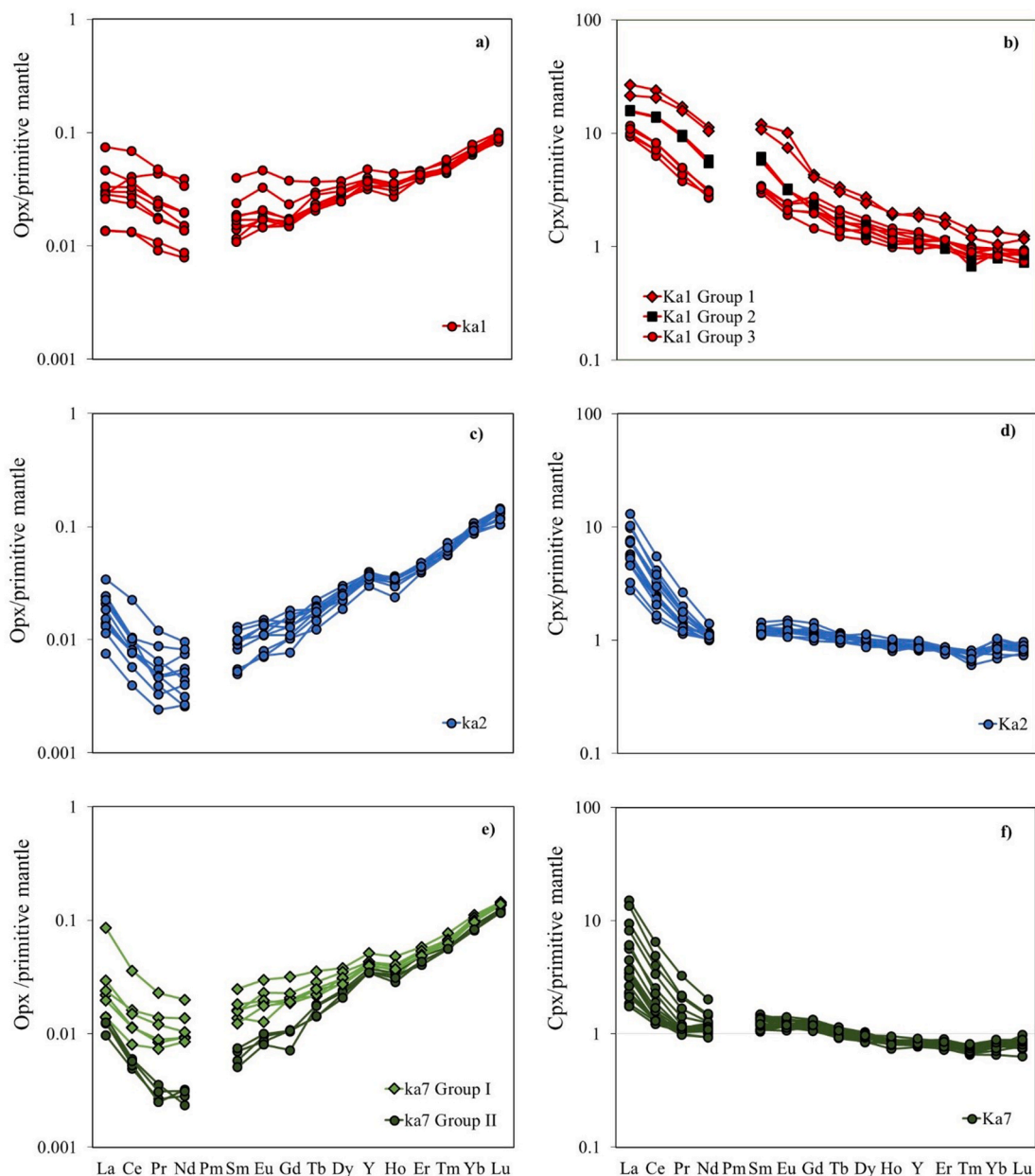
Fig. 5. Orthopyroxene and clinopyroxene REEs normalized to primitive mantle values of Palme and O'Neill (2014).

(Fig. 6a) show Th and U enrichments, a negative Nb anomaly, highly variable Sr concentrations (typically positive anomalies) and prominent positive Ti anomalies.

Overall, clinopyroxene and orthopyroxene REE plots show the same characteristic patterns (similar LREE to MREE enrichments in sample Ka1 and LREE enrichments in Ka2 and Ka7) and similar widespread compositions or shifts in the patterns except for sample Ka7 orthopyroxene, which shows a group with LREE-to MREE enrichments. The HREEs of orthopyroxene of Ka1 are more depleted than the other samples, whereas those of clinopyroxenes are more enriched. Clinopyroxenes from Ka1 show significant variation than orthopyroxene, particularly Nb. In general, Ka1 clinopyroxenes are more enriched than the other samples while orthopyroxenes are not and show more overlap.

4.3. Infrared spectra and H_2O concentrations

Average unpolarised infrared spectra of orthopyroxene and clinopyroxene show a range of absorption bands in the OH stretching/vibration region between 3800 and 3000 cm^{-1}. Orthopyroxenes from all samples have two prominent OH absorption bands at 3597 and ~3415 cm^{-1} (Fig. 7a). Additional weaker bands sometimes occur at ~3748 and ~3733 cm^{-1}. Sample Ka2 shows very weak bands at ~3524 cm^{-1} and Ka7 shows an additional prominent band at ~3519 cm^{-1} (Fig. 7a), which is not observed in the orthopyroxene from the other Kapsiki samples. Clinopyroxene from sample Ka1 exhibits a prominent band at 3638 cm^{-1} with a shoulder at 3685 cm^{-1}. Samples Ka2 and Ka7 show four bands: a variably intense band at 3682 cm^{-1}, a more consistently intense band at 3638 cm^{-1} and weaker bands at ~3527 and ~3448 cm^1. Bands at 3682 cm^{-1} can be attributed to the presence of amphibole lamellae (Ingrin et al., 1989; Della Ventura et al., 2007). Olivine spectra show no detectable OH bands (Fig. 7a). Calculated average H_2O contents (Table 1) in Kapsiki xenoliths are 277 ppm and 285 ppm for clinopyroxenes of Ka2 (3 clinopyroxenes) and Ka7 (4 clinopyroxenes). The H_2O contents in Ka1 clinopyroxenes are much lower (164 ppm). Clinopyroxene spectra containing amphibole bands at ~3682 cm^{-1} (Fig. 7b) were not considered during the calculations. Orthopyroxene H_2O
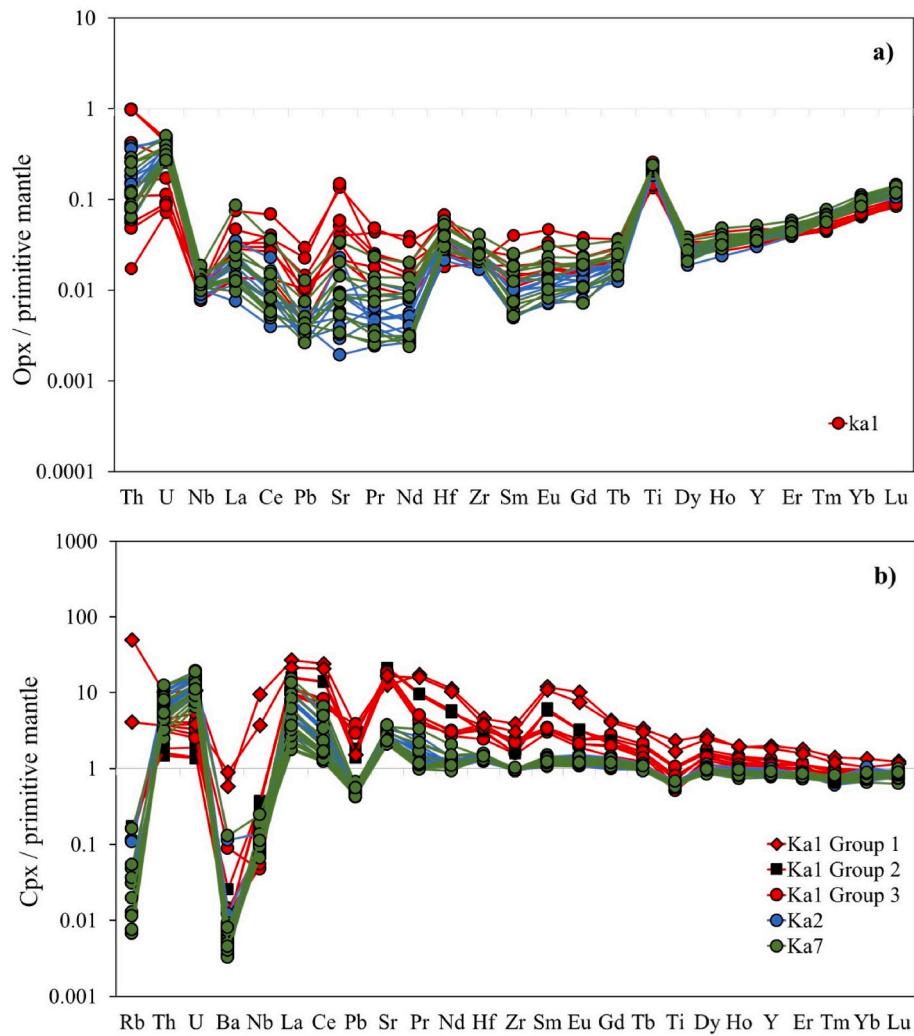
Fig. 6. a: Orthopyroxene and b) Clinopyroxene trace elements normalized to primitive mantle values of (Palme and O'Neill, 2014).

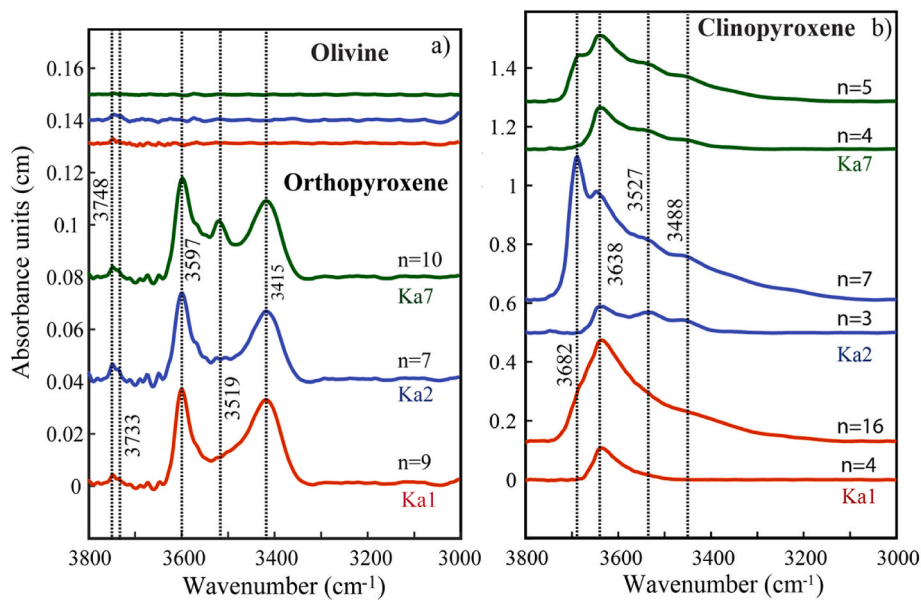**Fig. 7.** Average unpolarised FTIR spectra for a) olivine, orthopyroxene and b) clinopyroxenes from the Kapsiki peridotites, the peak at 3682 cm^{-1} corresponds to amphibole bands, Ka1 (red), Ka2 (blue), Ka7 (green). The water content values are in ppm and n is the number of grains analyzed. (For interpretation of the references to colour in this figure legend, the reader is referred to the Web version of this article.)

Table 1
FTIR characteristics and average hydrogen contents of orthopyroxene and clinopyroxene.

Sample	Orthopyroxene				Clinopyroxene			
	Absorbtion bands	Analyzed grains	Integral absorbance (cm^{-1})	H_2O (ppm)	Absorbtion bands	Analyzed grains	Integral absorbance (cm^{-1})	H_2O (ppm)
Ka1	3748, 3733, 3597, 3519, 3415	9	6.82 ± 0.78	46 ± 5	3682, 3638, 3527, 3488	5	11.42 ± 0.99	152 ± 16
Ka2	3748, 3733,3597,3415	7	6.00 ± 1.48	40 ± 8	3682, 3638, 3527, 3489	3	19.65 ± 5.12	277 ± 23
Ka7	3748, 3733, 3597, 3415	10	7.15 ± 1.46	48 ± 9	3682, 3638, 3527, 3489	4	20.24 ± 4.98	285 ± 48

contents in all samples are in the same range from 40 to 48 ppm with sample Ka7 showing the highest H_2O which could be as a result of the extra band at ~3519. Olivine shows very low H_2O contents below the limit of detection (<1ppm).

4.4. Equilibrium temperatures and oxygen fugacity

Temperatures were calculated using several geothermometers (Table 2). Olivine thermometers of De Hoog et al. (2010) assuming pressures of 1.5 GPa yielded T_{Ca-ol}, T_{Al-ol} and T_{Cr-ol} of 1000–1010 °C, 920–960 °C and 950–970 °C respectively. The use of olivine is advantageous over pyroxenes because chemical diffusion in olivine tends to be faster at least for Ca and probably Cr (Tollan et al., 2015) and hence olivine may therefore be more responsive to late-stage thermal events that are not recorded by pyroxene (De Hoog et al., 2010).

The Ca-in-orthopyroxene geothermometer of Brey and Köhler (1990) (T_{Ca-opx}) yielded temperatures of 890–900 °C. The olivine-spinel geothermometer (Jianping et al., 1995), which is an improved calibration of Fabriès, 1979, based on the partitioning of Mg^{2+} and Fe^{2+} between coexisting olivine and spinel gave temperatures of 930–980 °C. The olivine-spinel Al exchange thermometer of Coogan et al. (2014) yielded temperatures of 920–1060 °C.

Accurate application of the two-pyroxene thermometry relies on the assumption that orthopyroxene and clinopyroxene are in chemical equilibrium. Both Ka2 and Ka7 contain clinopyroxene that has considerably higher and more variable Mg# than coexisting orthopyroxene (Fig. 3a), implying that equilibrium in these samples was not achieved. Ka1 contains two populations of clinopyroxene, one of which has lower and more homogeneous Mg# similar to that of coexisting olivine and orthopyroxene. Although perfect equilibrium cannot be demonstrated, pyroxene thermometry will give an indication of differences in equilibration temperatures. As the pyroxene solvus is asymmetric, the variations in clinopyroxene compositions are more sensitive to temperature changes and hence the two-pyroxene thermometer provides information on the conditions of clinopyroxene formation. Application of the two-pyroxene thermometer of Brey and Köhler, 1990 gives temperatures of 881 and 1146 °C for the high and low Ca clinopyroxene populations, respectively.

The redox state of the Kapsiki xenoliths was estimated from the olivine-orthopyroxene-spinel oxygen geobarometer of Ballhaus et al. (1991). Estimated fO_2 (expressed as ΔlogFMQ, where FMQ corresponds to the fayalite-magnetite-quartz oxygen buffer) values of -0.39, -0.42 and -0.26 were obtained for Ka1, Ka2 and Ka7 respectively assuming pressures of 1.5 GPa and using temperatures calculated from the

olivine-spinel geothermometer of Jianping et al. (1995).

5. Discussion

5.1. Interpretation of textures in the xenoliths

The Kapsiki xenoliths show a sharp contact with the host basalt, which indicates rapid transport to the surface. However, a few clinopyroxene grains show spongy rims, which are randomly distributed within the sample, they show a sharp contact with the coexisting minerals and both the low and high CaO clinopyroxenes display the spongy rims. The coexisting minerals are devoid of any reaction textures. The origin of spongy textures in clinopyroxene remains under debate and have been attributed to, interactions of the xenolith with the host basalt (Shaw et al., 2006; Shaw and Dingwell, 2008), fluid/melt interactions before the transport of the xenolith to the surface (Bonadiman et al., 2005, 2008) or decompression induced melting (Su et al., 2011). The absence of relict melts along the spongy clinopyroxene argues against interactions with the host basalt. It is expected that interaction of the depleted mantle xenoliths with a basaltic melt would lead to clinopyroxene with a lower Mg# than olivine and orthopyroxene. However, the Mg# of clinopyroxene is always higher than coexisting olivine and orthopyroxene (Fig. 3a). Additionally, clinopyroxene shows similar trace element enrichment patterns as orthopyroxene, providing evidence for cryptic metasomatism. Therefore, we conclude that there is no evidence of secondary clinopyroxene due to interactions of the xenolith with the host basalt. Therefore, the observed textures and chemical trends are related to the evolution of the lithospheric mantle below the Kapsiki Plateau prior to the beginning of volcanic activity at 27–35 Ma as dated by Vincent and Armstrong (1973) and Dunlop (1983).

5.2. Partial melting

The removal of melt from the SCLM leads to both changes in mineralogy and chemistry with a transition from lherzolitic to harzburgitic assemblages. High olivine and orthopyroxene Mg# coupled with high spinel Cr# and the low pyroxene Al_2O_3 contents are common for the Kapsiki xenoliths. The compositional association of spinel Cr# and olivine Fo contents (Mg#) (Fig. 8a) defined by Arai (1994) and used to qualify melt extraction shows that sample Ka1 is the most refractory with average Mg# (Mg/(Mg + Fe)) of 0.92, but Ka2 and Ka7 are moderately refractory with average Mg# of 0.91. Such Mg# values are higher than typical mantle olivines (0.86–0.90) (Pearson et al., 2014) indicating substantial degrees of partial melting beneath the Kapsiki

Table 2
Temperature T (°C) estimates for Kapsiki xenoliths.

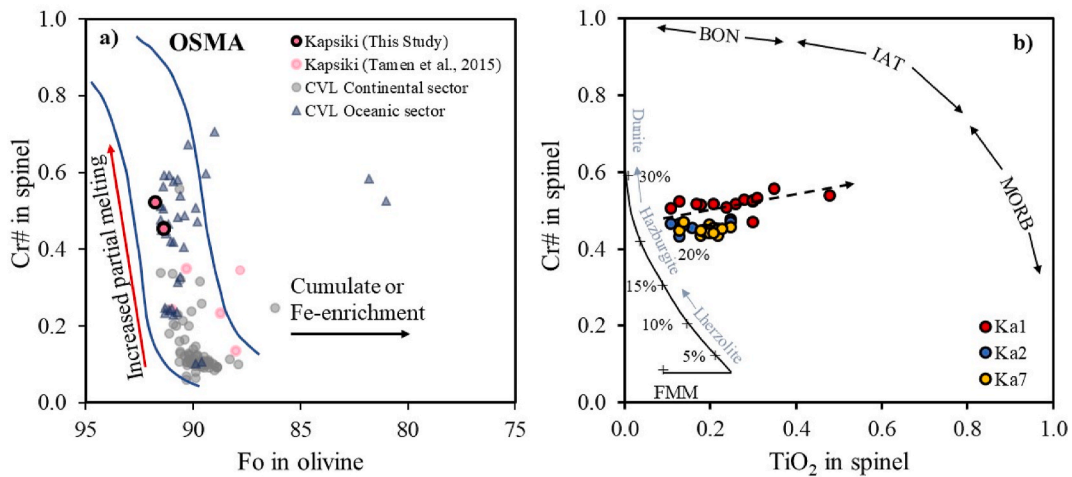| Samples	De Hoog et al., 2002			Coogan et al. (2014)	Jianping et al., 1995	Brey and Köhler, 1990	
	T_{Al-ol}	T_{Cr-ol}	T_{Ca-ol}	$T_{Al-ol-Sp}$	T_{ol-sp}	T_{Ca-opx}	$BKN_{Br\&Ko}$
Ka1	950 ± 10	973 ± 10	1011 ± 10	1061	980	897 ± 39	1146 (low Ca) 881 (high Ca)
Ka2	924 ± 12	954 ± 10	1002 ± 04	995	929	889 ± 23	837
Ka7	927 ± 09	953 ± 07	1005 ± 03	917	939	903 ± 45	864

Fig. 8. a: Mg# in olivine versus Cr# in spinel showing the compositional variation of Kapsiki peridotites and peridotites from the Cameroon Line (Temdjim et al., 2019; Njombie et al., 2018; Nkouandou et al 2015; Pintér et al., 2015; Matsukage and Oya, 2010; Caldeira and Munhá, 2002). b) Cr# in spinel versus TiO_2 in spinel.

plateau. The xenoliths thus represent the most refractory components in the continental CVL even though they are similar to xenoliths from the oceanic part of the line (Sao Tome; Caldeira and Munhá, 2002) (Fig. 8a).

To provide a quantitative estimate of the degree of partial melting, the methods of Hellebrand et al. (2001) and De Hoog et al. (2010) were applied, which are based on the Cr# of spinel and olivine respectively. The methods yielded 16–18% (spinel Cr#) and 12–16% (olivine Cr#) of partial melting, which is consistent with estimates of the degree of partial melting of olivine Mg# from Bernstein et al. (2007) of 15–30% for Mg# of 0.91–0.92. The high spinel Cr# could, however, also be due to modifications during interactions with fluids/melts (Gamal El Dien et al., 2019; Pearce et al., 2000). Extends of partial melting calculated for other CVL peridotites using the method of Hellebrand et al. (2001) yielded 1–14% (Liu et al., 2017) which are lower than for the Kapsiki xenoliths. Based on the model of Pearce et al. (2000), for spinel Cr# of 0.45–0.50 generated through partial melting, TiO_2 contents should be

less than 0.1 wt %. The Cr# versus TiO_2 contents in spinel (Fig. 8b) suggests that the Kapsiki xenoliths interacted with melts that led to an increase in TiO_2 contents.

A simple fractional partial melting model of orthopyroxene trace elements in a depleted mantle compared to measured orthopyroxene REE data (Fig. 9) was used to estimate the degree of partial melting. Orthopyroxene was used since clinopyroxene appears to be secondary (see below) and thus are not expected to record partial melting events. This model applies a non-modal fractional equation (Johnson et al., 1990) to a starting composition (DMM source composition from Workman and Hart, 2005), mineral mode and melting mode from Johnson et al., 1990 and partition coefficients ($D^{cpx/melt}$ for REE (Hart and Dunn, 1993), $D^{cpx/melt}$ for Pr, Eu, Gd, Tb, Ho, Tm (Ionov et al., 2002) and $D^{opx/melt}$, $D^{ol/melt}$, $D^{spl/melt}$ (Ionov et al., 2002 and references therein). HREEs (Lu–Ho) are consistent with >20% of partial melting. MREE through to LREE however, are progressively more enriched in the
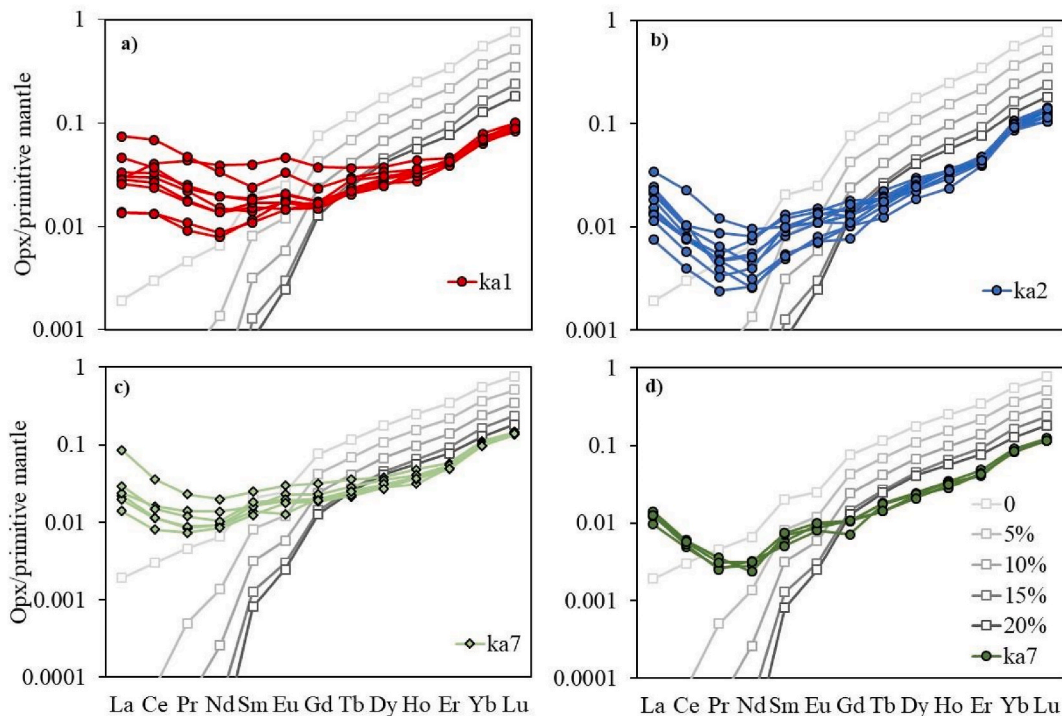

Fig. 9. Fractional partial melting model of orthopyroxene trace elements compared to Kapsiki orthopyroxene REE data.

Kapsiki orthopyroxene compared to the modelled compositions, clearly indicating reactions with relatively LREE and MREE enriched fluids after the depletion event(s). In the spinel stability field, olivine Mg# of 91.5 is approximately the point of clinopyroxene consumption, which will be at about 25% of partial melting (Hellebrand et al., 2001; Bernstein et al., 2007).

In summary, the Mg# of olivine and orthopyroxene and the HREE patterns of orthopyroxene are the most reliable tools to calculate the degree of melt depletion, while Cr# of spinel is likely to have been modified during subsequent metasomatism. Both the Mg#s and the HREE contents of orthopyroxene are consistent with 20–30% of melt extraction before the metasomatic refertilization. This means that parts of an ancient Archean/Proterozoic SCLM of lherzolitic composition were depleted by the extraction of basaltic melts leaving a mantle with little or no clinopyroxene of harzburgitic composition and depleted chemistry. The presence of such a highly depleted lithospheric subcontinental mantle indicates that old cratonic fragments persist and thus the proposed lithospheric delamination that led to abundant widespread magmatism at about 580 Ma (Bute et al., 2019) did not completely remove the lithospheric mantle below the northern extension of the CVL.

5.3. Metasomatism

The observed modal proportions of clinopyroxene (6–8%) are inconsistent with the proportions expected following the estimated 20–30% of partial melting experienced beneath Kapsiki, which indicates that the clinopyroxene must have been added subsequently. This is supported by the much smaller grain size of clinopyroxene (Fig. 2a, c). Features like highly variable pyroxene LREE enrichments and differing Mg# between clinopyroxene crystals in the same sample cannot be accounted for by partial melting and clearly indicate that the mantle must have undergone secondary processes. Trace element concentrations can be diagnostic of the type of metasomatic agent due to their differing behaviours, depending on the nature and source of the fluid and the method through which the fluid interacts with the mantle. Such considerable variability of elements within the same sample (Fig. 5) is a reflection of fluctuations during interactions which result in spatial changes in trace element concentrations due to chromatographic processes which are highly dependent on the relative mineral/melt partition coefficients of each of the elements (Ionov et al., 2002).

The Kapsiki xenoliths show evidence for both modal and cryptic metasomatism. Modal metasomatism is indicated by the presence of two groups of clinopyroxenes; a low and high Ca group (Fig. 3e and f), which are in interstitial positions (Fig. 2a) and are smaller in size than the coexisting minerals, which indicates that they crystallized at a later stage. The low Ca clinopyroxenes show evidence for metasomatism by carbonatite melts and record a higher temperature (1150 °C) while the high Ca types show more of interactions with carbonatite-silicate and silicate melts and lower temperatures (840–880 °C) (Table 2). Pyroxenes that recorded the higher temperatures were, therefore, the latest to be formed and this, was probably shortly before eruption. This shows that metasomatism by melts enriched in Ca and incompatible trace elements (Scott et al., 2014a) could be a precursor of xenolith formation and eruption.

Cryptic metasomatism, shown by geochemical fingerprints of fluids or melts are expressed as a gradation from low to high incompatible element enrichments in orthopyroxene and both groups of clinopyroxene (Figs. 5 and 6). These samples were far enough from the metasomatic source for the chromatographic effect to be recorded only in the LREE (Ionov et al., 2002; Uenver-Thiele et al., 2017) for Ka2 and Ka7, sample Ka1 was closer to the metasomatic source because even the MREEs were perturbed. In a rock with a lherzolite lithology, clinopyroxene melts preferentially to olivine and orthopyroxene during decompression of the mantle, which means that clinopyroxene can easily be exhausted at low degrees of partial melting (~25%) leaving an olivine-orthopyroxene residue (Walter, 2003). As such, orthopyroxene

would probably be more sensitive to metasomatism (Scott et al., 2014b, 2016). Orthopyroxenes from all samples show the same style of metasomatic enrichment as clinopyroxenes in REEs in all samples.

Selective enrichment in Th, U, Sr and LREE in samples Ka2 and Ka7 depict interactions with a metasomatic agent at low melt/rock ratios (Grégoire et al., 2009). Alternatively, additional MREE enrichments in Ka1 point to possible infiltration of a fluid or melt (Grégoire et al., 2005) at higher melt rock ratios. The general enrichment in all elements especially Rb, Ba, Sr, Nb and MREEs) of group 1 clinopyroxene (Fig. 5b, c, f) of sample Ka1 is also consistent with interactions with fluids or melts of different compositions.

5.4. Fluid/melt composition

The nature and composition of metasomatising fluids can be constrained from the mineralogic and chemical compositions of xenoliths, as such, trace element patterns and ratios are very important tools that can be used to discriminate different metasomatic fluids/melts. However, the occurrence of different trace element enrichment patterns in the Kapsiki xenoliths complicates their interpretation and brings in the possibility of multiple metasomatic agents. It is important when interpreting normalized mineral compositions to consider whether element anomalies are due to secondary processes (e.g., fluid metasomatism) or whether they are an artefact of relative compatibility. For example, the negative anomalies in Rb and Ba are typical features of clinopyroxene and are due to their greater incompatibility relative to neighbouring elements.

Mantle metasomatism has generally been ascribed to infiltration by silicate melts (Zangana et al., 1999), carbonatite melts (Rudnick et al., 1993; Yaxley et al., 1998; Shu and Brey, 2015), aqueous or CO_2-rich fluids (O'Reilly and Griffin, 1988; Downes, 2001) and subduction-related fluids/melts (Pearce et al., 2005). Silicate melts are characterized by high concentrations of incompatible trace elements (Th, U, Ba, Nb, Sr, K, LREEs) (Zangana et al., 1999). Carbonatite melts are more enriched in moderately to highly incompatible trace elements (Rb, Th, U, Ba, Sr, K, Cs, LREEs), Eu and are depleted in HFSEs (Zr, Hf, Ti, Nb, Ta) compared to silicate melts (Lenoir et al., 2000; Dasgupta and Hirschmann, 2006; Liu et al., 2020). Additionally, high La/Yb, Ca/Al, Zr/Hf and low Ti/Eu ratios are characteristic for carbonatite melts (Rudnick et al., 1993). Fractionated incompatible trace elements accompanied by positive LILE, in particular, Pb plus negative HFSE anomalies, point to a mantle that has been metasomatised by subduction-related fluids (Pearce et al., 2005). Fig. 10 shows a series of plots using diagnostic trace elements (primitive mantle normalized values) of the clinopyroxenes, compared with published data from peridotites where the tectonic setting (intraplate, subduction or abyssal peridotite) is known. We assume, therefore, that the trace element compositions from these studies are representative of the type of fluids/processes that characterize each tectonic environment. The Sr–Nd diagram effectively separates the abyssal and subduction-related peridotites from the intraplate peridotites. These trace element plots show that the Kapsiki xenoliths are different from xenoliths from the abyssal and subduction settings and they fall in the same domain as those from intraplate settings. Within the intraplate group, the Th–La diagram nicely separates the continuous trends of Ka2, Ka7 from Ka1, which shows three distinct groups of compositions (Fig. 10). Negative Nb anomalies are inconsistent with metasomatism by alkaline melt, but combined with strong enrichments in U and Th indicate the involvement of a carbonatite fluid component.

The discrimination of silicate and carbonatite melts using Ti/Eu vs (La/Yb)$_N$ in clinopyroxene (Coltorti et al., 1999) systematics shows that one group of Ka1 clinopyroxene falls in the carbonatite field (Fig. 11a). The second group alongside Ka2 and Ka7 clinopyroxenes do not fall within any of the defined fields. A few Ka2 and Ka7 clinopyroxenes grains are however characterized by low (La/Yb)$_N$ and high Ti/Eu ratios, indicating a dominance of interactions with basaltic melts (Xu et al.,
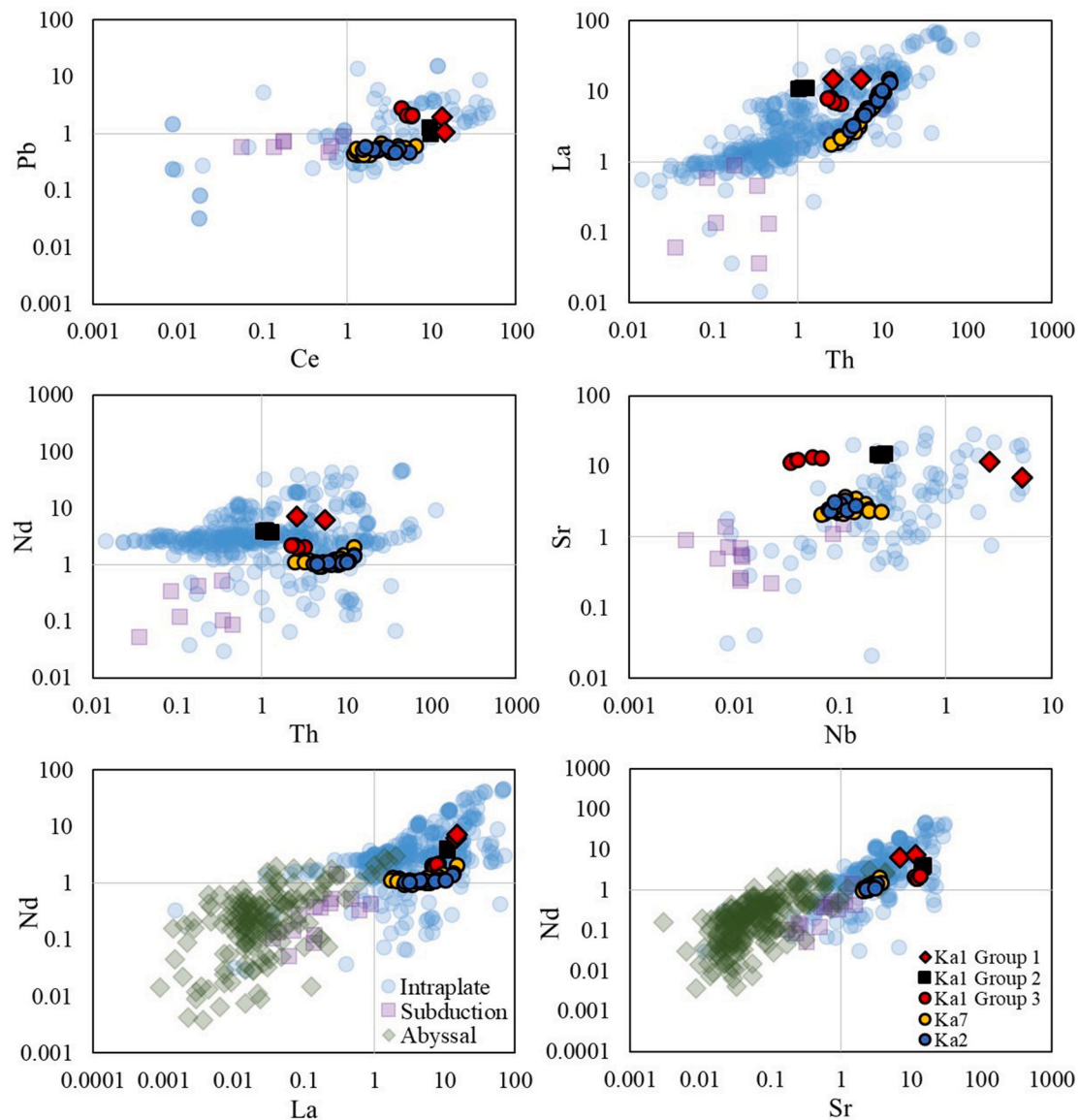
Fig. 10. Trace element plots of clinopyroxene compared to literature data from intra plate (McCoy-West et al., 2015; Scott et al., 2014a, 2016; Uenver-Thiele et al., 2017), subduction (Bénard and Ionov, 2013; Tollan et al., 2017) and Abyssal settings (Warren, 2016). The data is provided in Supplementary material, Appendix C. Values are normalized to primitive mantle values of Palme and O'Neill (2014).

2003). Generally, clinopyroxenes from other localities along the CVL, e. g. Befang (Tedonkenfack et al., 2021) and Nyos (Liu et al., 2017; Teitchou et al., 2011) show low (La/Yb)$_N$ and high Ti/Eu ratios and have been ascribed to metasomatism by depleted MORB mantle. Those from Nyos show clear evidence for both silicate and carbonatite metasomatism but differ from most of the Kapsiki clinopyroxenes which do not show metasomatism by well-defined end-member fluids. In the discrimination diagram of Zr/Hf vs Ti/Eu, Kapsiki samples were compared to those from the French Massif Central (FMC) (Uenver-Thiele et al., 2017) (Fig. 11b) where trace elements were used in conjunction with oxidation state measurement. The Kapsiki xenoliths are similar to the FMC xenoliths as both display evidences for both interactions with carbonatite-silicate and silicate melts. This correlates well with the results obtained from the (La/Yb)$_N$ and Ti/Eu plot. The Kapsiki xenoliths also show oxidation state values at the lower end of those obtained for the FMC xenoliths which range from FMQ -0.47 to FMQ +1.66. The heterogeneity of the non-cratonic SCLM in terms of oxidation state values implies an overprint by different types and intensities of metasomatism which therefore reflect complex processes (Foley, 2010;

Uenver-Thiele et al., 2017).

Metasomatism by melts of undefined composition could result from mixing of melts of varying proportions or a gradual overprinting of one fluid type by another (Su et al., 2010). Samples with the lowest (La/Yb)$_N$ values are therefore representative of an approximate end-member, which has been modified by silicate melts with a minimum influence from carbonatites.

Ti/Sr ratios of Ka1 samples range from 1 to 11, Ka2 and Ka7 ratios are much higher in the range of 9–18. Clinopyroxene metasomatised by carbonatite melts worldwide show low Ti/Sr ratios (Scott et al., 2014a: Ti/Sr = 1–5, Norman, 1998 = 2–4; Fig. 11c). They are similar to clinopyroxenes from the FMC (Uenver-Thiele et al., 2017), and the CVL (Tedonkenfack et al., 2021; Liu et al., 2017; Teitchou et al., 2011), but generally show more carbonatitic affinity than CVL clinopyroxenes (Fig. 11c). Ca/Al major element ratios (Rudnick et al., 1993) in clinopyroxenes is also an important geochemical metasomatic tracer. Results from experimental studies show that low Ca/Al values <5 record interactions with silicate melts (Wang et al., 2010; Yaxley and Green, 1998) while Ca/Al ratios >5 were attributed to carbonatite interactions
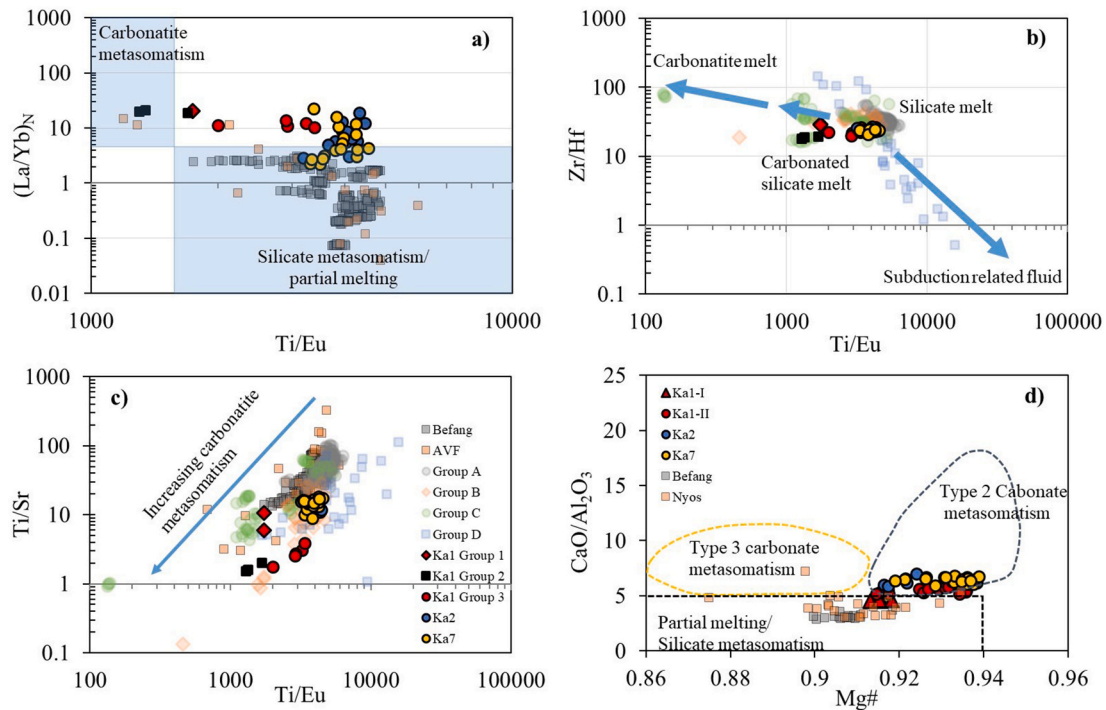
Fig. 11. a) Plot of Ti/Eu vs chondrite normalized (McDonough and Sun, 1995) La/Yb in clinopyroxenes, compared to clinopyroxenes from Befang (Tedonkenfack et al., 2021) and Nyos (Liu et al., 2017; Teitchou et al., 2011), fields for carbonatite and silicate metasomatism are from Coltorti et al. (1999). b. c) Plot of Ti/Eu vs Zr/Hf and Ti/Sr vs Ti/Eu in clinopyroxenes compared samples from the French Massif Central (Uenver-Thiele et al., 2017), Groups A-D represent the degree of LREE to MREE enrichments in clinopyroxene. d) Ca/Al vs Mg# in clinopyroxene. Fields are from Zong and Liu, 2018).

(Dalton and Wood, 1993; Klemme et al., 1995; Brey et al., 2008; Gervasoni et al., 2017). Ca/Al values of 4–8 are also consistent with metasomatism induced by small amounts of volatile-rich melts (Xu et al., 2003). Plots of Ca/Al versus Mg# (Fig. 11d) show that most of the Kapsiki xenoliths straddle the silicate-carbonatite boundary and most of them fall in the type 2 carbonatite field defined by Zong and Liu, 2018) and are similar to other peridotites in Cenozoic volcanic rocks worldwide. The CVL xenoliths fall in the silicate metasomatism domain while a few xenoliths from Nyos straddle the boundary between silicate metasomatism and type 3 carbonatite metasomatism (Fig. 11d). Type 2 carbonatite metasomatism is characterized by high Mg# (>91) and Ca/Al ratios of 5–8 while type 3 shows lower Mg# (0.86–0.91) and a narrow range of Ca/Al ratios (5-11) (Zong and Liu, 2018).

Kapsiki xenoliths represent depleted residues (high Mg#) after the extraction of basaltic melts but have close to or modal compositions of lherzolites. This shows evidence for metasomatism by melts enriched in Ca and incompatible trace elements (Scott et al., 2014a) which led to the formation of the secondary clinopyroxenes. A puzzling feature is the observation of very high Mg# in the metasomatic clinopyroxene (0.92–0.94) compared to the residual olivine and orthopyroxene (0.91–0.92). Primary carbonatite melts in equilibrium with peridotites have an Mg# of 0.85–0.90 (Hammouda and Keshav, 2015) that is significantly higher than the Mg# of 0.70 for primary silicate melts. We speculate that the reaction of such a carbonate melt component in a mixed carbonatite-silicate melt with a depleted peridotite will result in clinopyroxene with an elevated Mg#.

All the discrimination diagrams (Figs. 10 and 11) for mantle metasomatism are based on clinopyroxene compositions. This is reasonable as clinopyroxene is newly formed during the metasomatic process and displays the highest concentrations of incompatible trace elements among the mantle phases. The drawback of this approach is that only clinopyroxene bearing samples can be classified. Our study of the Kapsiki xenoliths shows that orthopyroxene experienced cryptic metasomatism and the incompatible trace element patterns display some

similar features to the clinopyroxene patterns (Fig. 6). Therefore, it is proposed that Sr–Nd and Th–La discrimination diagrams for the classification of metasomatic agents might be possible also using orthopyroxene compositions. Also, olivine shows some promising trends. However, many of these trace elements are strongly modified by subsolidus cooling (De Hoog et al., 2010; Tollan et al., 2017) and comprehensive databases for such classifications are still missing.

In summary, major and trace element systematics of the Kapsiki clinopyroxenes provides clear evidence for metasomatism by varying proportions of carbonatite and silicate melts. This metasomatism may have been a single event with a hybridized melt, or separate events produced by variable overprinting of the end member compositions (Beard et al., 2007). It is not possible to distinguish between these two options based on the available data.

5.5. Implication of water budget

NAMs in the Earth's mantle contain variable amounts of hydrogen structurally bond as hydroxyl (Bell and Rossman, 1992) in their crystal lattice, thus can be a significant hydrogen reservoir (Ingrin and Skogby, 2000). Water contents and the hydrogen activity of fluids in the mantle show substantial variability and can largely influence the physical and chemical properties of the mantle (Van der Lee et al., 2008), hence, play an important role in understanding mantle dynamics (Bonadiman et al., 2009). Metasomatic agents that interact with the mantle can have highly variable H_2O contents and activities (aH_2O). For example, subduction zone fluids are likely to be highly enriched in H_2O with high aH_2O, whereas carbonatitic fluids should have much higher CO_2 contents and thus lower aH_2O. Hydrogen in NAMs may therefore be a powerful tool for distinguishing between some of these different metasomatic components. Despite this, most studies trying to link metasomatism with hydrogen in minerals struggle to find straightforward links. One reason for this may be that H diffuses significantly faster than other trace elements, and thus may re-equilibrate post-metasomatism, eradicating any

original correlations with co-enriched/depleted elements (e.g., Denis et al., 2018). Another reason is that the hydrogen contents of NAMs may not necessarily have a direct correlation with the hydrogen contents of fluids, since H incorporation in NAMs is strongly dependent on the availability of defects which is directly linked to parameters such as pressure, aH$_2$O, mineral chemistry and fO$_2$ (Berry et al., 2005; Ardia et al., 2012; Tollan et al., 2017).

Olivines from the Kapsiki xenoliths show no OH stretching bands and the H$_2$O contents are therefore estimated to be <1 ppm. The very low olivine H$_2$O content is a common feature of peridotite xenoliths and has been interpreted to be due to rapid diffusion of H in olivine during transport to the surface by H$_2$O-undersaturated magmas (Peslier and Luhr, 2006; Demouchy et al., 2006; Xia et al., 2010; Tian et al., 2017). Alternatively, low water contents caused by depleted chemistry (particularly low Ti and Cr contents and high Na/Cr) and low aH$_2$O could have inhibited H incorporation (Tollan et al., 2017, 2018). The Kapsiki olivines are different from other olivines along the CVL (Pintér et al., 2015) which show characteristic OH stretching bands at 3573 and 3525 cm^{-1} (Ti substitution), 3229 cm^{-1} (Mg substitution) and consequently higher H$_2$O contents (0.6–6.6 ppm). Tollan et al., 2018 showed that when interacting with a pure H$_2$O fluid (aH$_2$O = 1) at 1.5 GPa, the 5–10 μg/g Ti measured in the Kapsiki olivines studied here should generate easily detectable bands at 3572 and 3525 cm^{-1} (3–6 ppm H$_2$O). This is therefore consistent with the expected much lower aH$_2$O of the metasomatic agents beneath Kapsiki.

Orthopyroxene FTIR spectra show five OH stretching bands. The most prominent are at ~3600, 3520 and 3415 cm^{-1} and the position of the bands are similar to reported orthopyroxene spectra (Pintér et al., 2015) along the Cameroon Volcanic Line and other localities (Patkó et al., 2019; Demouchy et al., 2015; Li et al., 2015; Bonadiman et al., 2009). The most striking feature in these spectra and the major difference with those from the CVL is the stretching region at ~3520 cm^{-1}, which is absent in Ka1 and Ka2 and present in Ka7 (Fig. 7a). Also, the bands at 3415 cm^{-1} are more intense in the Kapsiki samples. In orthopyroxene, two main peaks (3600 and 3420 cm^{-1}) are insensitive to oxygen fugacity, however, the peak at ~3525 cm^{-1} has been shown to increase with increasing fO$_2$ (Tollan and Hermann, 2019). This is consistent with observations in the Kapsiki sample with Ka7 showing the highest fO$_2$ and the most prominent bands at 3519 cm^{-1}. The specific substitution mechanism related to the presence of the OH stretching regions at 3600 and 3420 cm^{-1} has been linked to the presence of hydrated Si vacancies and tetrahedral Al, based on experimental studies (Prechtel and Stalder, 2012). The orthopyroxene spectra can also give information on the associated tectonic setting, for example, the spectra from off-craton intraplate (this study; Li et al., 2008; Grant et al., 2007b; Bonadiman et al., 2009), cratonic (Peslier et al., 2012), arc (Peslier et al., 2002; Tollan and Hermann, 2019) and abyssal (Skogby et al., 1990; Gose et al., 2009; Schmädicke et al., 2011) orthopyroxene are distinctly different. Calculated average orthopyroxene hydrogen contents range from 40 to 50 ppm are lower than in most peridotites from off-cratonic settings (Peslier and Luhr, 2006; Demouchy et al., 2006; Grant et al., 2007b; Pintér et al., 2015). The low values obtained could be influenced by the depleted chemistry (low Al$_2$O$_3$) (Tollan and Hermann, 2019) of the Kapsiki orthopyroxenes.

Clinopyroxenes (Fig. 7b) show two distinct spectra in all samples; the first type with prominent OH stretching bands at ~3638 cm^{-1} and two less prominent at ~3525 and ~3488 cm^{-1}. The second spectra type shows an additional band at ~3682 cm^{-1} which can be attributed to the presence of amphibole lamellae in clinopyroxene (Della Ventura et al., 2007). As in the case of orthopyroxene, substitution mechanisms in clinopyroxenes are also not yet well constrained but are thought to be principally controlled by coupled substitution of H with tetrahedral Al (Stalder and Ludwig, 2007; O'Leary et al., 2010).

The H$_2$O concentrations of both orthopyroxene (40–48 ppm) and clinopyroxene (164–285 ppm) are on the low end of the global distribution of compositions (Demouchy and Bolfan-Casanova, 2016). This is somewhat surprising given the strong evidence for modal metasomatism and enrichment of highly incompatible elements. We suggest that the principle explanation for this is that the contribution of carbonatite melt resulted in a much lower aH$_2$O compared to a typical metasomatising agent, and considering the strong relationship between aH$_2$O and H$_2$O solubility (Tollan et al., 2017). The H$_2$O concentration ratios between clinopyroxene and orthopyroxene (R$_{cpx/opx}$) range from 3 to 7 and are much higher than the value proposed to reflect equilibrium partitioning (R$_{cpx/opx}$ = 2.1) by Demouchy and Bolfan-Casanova, 2016. This could indicate that the mantle below the region did not attain a state of equilibration before eruption, orthopyroxenes preferentially lost H$_2$O compared to clinopyroxenes during ascent or that substantially different substitution mechanisms are operating in the Kapsiki crystals. The major element composition of Kapsiki pyroxenes are unremarkable compared to the global mantle array, discounting the latter option. Furthermore, core-rim H$_2$O measurements in orthopyroxene grains show no systematic variation, indicating that H-loss during ascent is also an unlikely explanation. A possible explanation is that orthopyroxene is a residual phase, whose H$_2$O contents were modified through H diffusion (decoration) during metasomatism.

Clinopyroxene on the other hand was modally added through crystallization, and the OH defects and H$_2$O concentrations thus reflect crystallization processes, rather than H diffusion/vacancy decoration. These different mechanisms of incorporating H have been shown to result in quite substantial differences in stable defects and H$_2$O solubility (Tollan et al., 2018). This study, therefore, highlights the vital importance of establishing the origin of each mineral phase and mechanisms of H incorporation when interpreting the H$_2$O concentrations.

6. Conclusion

Detailed mineral major and trace element concentrations together with hydrogen contents were analyzed in clinopyroxene bearing spinel harzburgites from the Kapsiki plateau. The results obtained show evidences for an ancient melt depletion event, documented as high Mg# of 0.91–0.92 in olivine and orthopyroxene, high Cr# of 0.4–0.55 in spinel and steep HREE patterns in orthopyroxene. All indicators provide consistent evidence for 20–30% melt depletion corresponding to conditions whereby clinopyroxene is lost from the residue.

The harzburgites also show additional evidence for multiple metasomatic episodes resulting in different enrichment trends in the studied samples and bulk addition of clinopyroxene. At least two episodes of clinopyroxene addition/modification are documented.

Additionally, the generally low water contents obtained together with the mineral chemistry predicts a dominance of metasomatism by carbonatite-silicate melts, even though there is evidence for minor carbonatite metasomatism. In both melts the H$_2$O activity was likely lower than in silicate melts, resulting in a less pronounced H$_2$O enrichment. Clinopyroxene has a significantly higher Mg# of 0.92–0.94 than olivine and orthopyroxene, which is also interpreted as a characteristic signature of metasomatism by carbonate melts.

A series of discrimination diagrams were developed based on clinopyroxene trace element compositions to distinguish between different types of clinopyroxene in mantle peridotites. The Sr vs. Nd diagram effectively separates abyssal and subduction-related peridotites from intraplate peridotites, whereas the Th vs La diagram provides insights into different types of metasomatism in an intraplate setting. Our study shows that orthopyroxene that experienced cryptic metasomatism displays comparable features. This opens the possibility to also use orthopyroxene as an indicator for mantle metasomatic processes once a comprehensive database is available.

Declaration of competing interest

The authors declare that they have no known competing financial interests or personal relationships that could have appeared to influence

the work reported in this paper.

Appendix A. Supplementary data

Supplementary data to this article can be found online at https://doi.org/10.1016/j.jafrearsci.2022.104483.
Palme and O'Neill (2014).

References

Adjia, H.Z., Villiéras, F., Kamga, R., Thomas, F., 2013. Mineralogy and physico-chemical properties of Alluvial Clays from the Far-North region of Cameroon: a tool for an environmental problem. Int. J. Water Resour. Environ. Eng. 5, 54–66.

Arai, S., 1994. Characterization of spinel peridotites by olivine-spinel compositional relationships: review and interpretation. Chem. Geol. 113 (3–4), 191–204.

Ardia, P., Hirschmann, M.M., Withers, A.C., Tenner, T.J., 2012. H2O Storage Capacity of Olivine at 5–8 GPa and Consequences for Dehydration Partial Melting of the Upper Mantle, pp. 345–348.

Ballhaus, C.G., Berry, R.F., Green, D.H., 1991. High-pressure calibration of the olivineorthopyroxene-spinel oxygen barometer, implications for the oxidation state of the upper mantle. Contrib. Mineral. Petrol. 107, 7–40.

Beard, A.D., Downes, H., Mason, P.R.D., Vetrin, V.R., 2007. Depletion and enrichment processes in the lithospheric mantle beneath the Kola Peninsula (Russia): evidence from spinel lherzolite and wehrlite xenoliths. Lithos 94 (1–4), 1–24.

Bell, D.R., Ihinger, P.D., Rossman, G.R., 1995. Quantitative analysis of trace OH in garnet and pyroxenes. Am. Mineral. 80, 465–474.

Bell, D.R., Rossman, G.R., 1992. Water in Earth's mantle: the role of nominally anhydrous minerals. Science 255 (5050), 1391–1397.

Bell, D.R., Rossman, G.R., Maldener, J., Endisch, D., Rauch, F., 2003. Hydroxide in olivine: a quantitative determination of the absolute amount and calibration of the IR spectrum. J. Geophys. Res. Solid Earth 108, 2105.

Bénard, A., Ionov, D.A., 2013. Melt–and fluid–rock interaction in supra-subduction lithospheric mantle: evidence from andesite-hosted veined peridotite xenoliths. J. Petrol. 54, 2339–2378.

Bernstein, S., Kelemen, P.B., Hanghøj, K., 2007. Consistent olivine Mg# in cratonic mantle reflects Archean mantle melting to the exhaustion of orthopyroxene. Geology 35 (5), 459.

Berry, A.J., Hermann, J., O'Neill, Hugh, S.C., Foran, G.J., 2005. Fingerprinting the water site in mantle olivine. Geology 33 (11), 869.

Bonadiman, C., Coltorti, M., Beccaluva, L., Siena, F., 2005. Kimberlite-like metasomatism and 'garnet signature' in spinel-peridotite xenoliths from sal, Cape Verde Archipelago: Relics of a subcontinental mantle domain within the Atlantic oceanic lithosphere? J. Petrol. 46, 2465–2493.

Bonadiman, C., Coltorti, M., Beccaluva, L., Siena, F., 2008. Mantle metasomatism vs. host magma interaction: the ongoing controversy. Geophys. Res. Abstr. 10. EGU2008-A-09723.

Bonadiman, C., Hao, Y., Coltorti, M., Dallai, L., Faccini, B., Huang, Y., Xia, Q., 2009. Water contents of pyroxenes in intraplate lithospheric mantle. Eur. J. Mineral 21 (3), 637647.

Brey, G.P., Bulatov, V.K., Girnis, A.V., Lahaye, Y., 2008. Experimental melting of carbonated peridotite at 6–10 GPa. J. Petrol. 49, 797–821.

Brey, G.P., Köhler, T.P., 1990. Geothermobarometry in natural four-phase lherzolites: Part II. New thermobarometers and practical assessment of existing thermobarometers. J. Petrol. 31, 1353–1378.

Bute, S.I., Yang, X.-Y., Cao, J., Liu, L., Deng, J.-H., Haruna, I.V., Girei, M.B., Abubakar, U., Akhtar, S., 2019. Origin and tectonic implications of ferroan alkali-calcic granitoids from the Hawal Massif, east-eastern Nigeria terrane: clues from geochemistry and zircon U-Pb Hf isotopes. Int. Geol. Rev. 62, 129–152.

Caldeira, R., Munhá, J.M., 2002. Petrology of ultramafic nodules from Sao Tomé Island, Cameroon Volcanic line (oceanic sector). J. Afr. Earth Sci. 34, 231–246.

Coltorti, M., Bonadiman, C., Hinton, R.W., Siena, F., Upton, B.G.J., 1999. Carbonatite metasomatism of the oceanic upper mantle: evidence from clinopyroxenes and glasses in ultramafic xenoliths of Grande Comore, Indian Ocean. J. Petrol. 40, 133–165.

Coogan, L.A., Saunders, A.D., Wilson, R.N., 2014. Aluminum-in-olivine thermometry of primitive basalts: evidence of an anomalously hot mantle source for large igneous provinces. Chem. Geol. 368, 1–10.

Dalton, J.A., Wood, B.J., 1993. The composition of primary carbonate melts and their evolution through wall rock reaction in the mantle. Earth Planet Sci. Lett. 119, 511–525.

Dasgupta, R., Hirschmann, M.M., 2006. Melting in the Earth's deep upper mantle caused by carbon dioxide. Nature 440 (7084), 659–662.

De Hoog, J.C.M., Gall, L., Cornell, D.H., 2010. Trace element geochemistry of mantle olivine and application to mantle petrogenesis and geothermobarometry. Chem. Geol. 270, 196–215.

Della Ventura, G., Oberti, R., Hawthorne, F.C., Bellatreccia, F., 2007. FTIR spectroscopy of Ti-rich pargasites from Lherz and the detection of O2 at the anionic O3 site in amphiboles. Am. Mineral. 92 (10), 1645–1651.

Demouchy, S., Bolfan-Casanova, N., 2016. Distribution and transport of hydrogen in the lithospheric mantle: a review. Lithos 240, 402–425.

Demouchy, S., Ishikawa, A., Tommasi, A., Alard, O., Keshav, S., 2015. Characterization of hydration in the mantle lithosphere: peridotite xenoliths from the Ontong Java Plateau as an example. Lithos 212–215, 189–201.

Demouchy, S., Jacobsen, S.D., Gaillard, F., Stern, C.R., 2006. Rapid magma ascent recorded by water diffusion profiles in mantle olivine. Geology 34 (6), 429.

Denis, C.M.M., Demouchy, S., Alard, O., 2018. Heterogeneous hydrogen distribution in orthopyroxene from veined mantle peridotite (San Carlos, Arizona). In: Impact of Meltrock Interactions. Lithos. S0024493718300112.

Déruelle, B., Ngounouno, I., Demaiffe, D., 2007. The "Cameroon hot line" (CHL): a Unique example of active alkaline intraplate structure in both oceanic and continental lithospheres. Compt. Rendus Geosci. 339, 589–600.

Déruelle, B., Ngounouno, I., Bardintzeff, M.J., 2001. Werlites et pyroxénites en nodules dans les basaltes du Mt. Cameroun: évidence d'un métasomatisme mantellique. J. Soc. Géosci. d'Afriq. 1, 90–91.

Doucet, L.S., Peslier, A.H., Ionov, D.A., Brandon, A.D., Golovin, A.V., Goncharov, A.G., Ashchepkov, I.V., 2014. High water contents in the Siberian cratonic mantle linked to metasomatism: an FTIR study of Udachnaya peridotite xenoliths. Geochem. Cosmochim. Acta 137, 159–187.

Downes, H., 2001. Formation and modification of the shallow subcontinental lithospheric mantle; a review of geochemical evidence from ultramafic xenolith suites and tectonically emplaced ultramafic massifs of western and central Europe. J. Petrol. 42, 233–250.

Dunlop, H.M., 1983. Strontium Isotope Geochemistry and Potassium ± Argon Studies on Volcanic Rocks from the Cameroon Line, West Africa. PhD Thesis. Univ., Edinburgh, p. 347p.

Eggins, S.M., Rudnick, R.L., McDonough, W.F., 1998. The composition of peridotites and their minerals: a laser-ablation ICP–MS study Earth Planet, 1998 Sci. Lett. 154 (1), 53–71.

Fabriès, J., 1979. Spinel-Olivine geothermometry in peridotites from ultramafic complexes. Contrib. Mineral. Petrol. 69, 329–336.

Ferré, E., Gleizes, G., Caby, R., 2002. Obliquely convergent tectonics and granite emplacement in the Trans-Saharan belt of Eastern Nigeria: a synthesis. Precambrian Res. 114, 199–219.

Fitton, J.G., 1983. Active versus passive continental rifting: evidence from the WestAfrican rift system. Tectonophysics 93, 473–481.

Foley, S.F., 2010. A reappraisal of redox melting in the Earth's mantle as a function of tectonic setting and time. J. Petrol. 52, 1363–1391.

Gamal El Dien, H., Arai, S., Doucet, L., Li, Z., Kil, Y., Fougerouse, D., Reddy, S.M., Saxey, D.Y., Hamdy, M., 2019. Cr–spinel records metasomatism not petrogenesis of mantle rocks. Nat. Commun. 5103.

Ganwa, A.A., Klötzli, U.S., Diguim Kepnamou, A., Hauzenberger, C., 2016. Multiple Ediacaran tectono-metamorphic events in the Adamawa-Yadé domain of the central Africa fold belt: insight from the zircon U–Pb LAM-ICP-MS geochronology of the metadiorite of Meiganga (Central Cameroon). \ Geol. J. 1–14.

Gervasoni, F., Klemme, S., Rohrbach, A., Grützner, T., Berndt, J., 2017. Experimental constraints on mantle metasomatism caused by silicate and carbonate melts. Lithos 282–283, 173–186.

Gose, J., Schmädicke, E., Beran, A., 2009. Water in enstatite from Mid-Atlantic Ridge peridotite: evidence for the water content of sub-oceanic mantle? Geology 37 (6), 543–546.

Goussi, Ngalamo, J.F., Sob, M., Bisso, D., Abdelsalam, M.G., Atekwana, E., Ekodeck, G.E., 2018. Lithospheric structure beneath the Central Africa Orogenic Belt in Cameroon from the analysis of satellite gravity and passive seismic data. Tectonophysics 745, 326–337.

Grant, K.J., Kohn, S.C., Brooker, R.A., 2007. The partitioning of water between olivine, orthopyroxene and melt synthesised in the systemalbite-forsterite-H2O. Earth Planet Sci. Lett. 260, 227–241.

Grégoire, M., Langlade, J.A., Delpech, G., Dantas, C., Ceuleneer, G., 2009. Nature and evolution of the lithospheric mantle beneath the passive margin of East Oman: evidence from mantle xenoliths sampled by Cenozoic alkaline lavas. Lithos 112/3, 203–216.

Grégoire, M., Tinguely, C., Bell, D.R., Le Roex, A.P., 2005. Spinel lherzolite xenoliths from the Premier kimberlite (Kaapvaal craton, South Africa): nature and evolution of the shallow upper mantle beneath the Bushveld complex. Lithos 84, 185–205.

Griffin, W.L., O'Reilly, S.Y., Afonso, J.C., Begg, G.C., 2008. The composition and evolution of lithospheric mantle: a Re-evaluation and its tectonic implications. J. Petrol. 50 (7), 1185–1204.

Hammouda, T., Keshav, S., 2015. Melting in the mantle in the presence of carbon: review of experiments and discussion on the origin of carbonatites. Chem. Geol. 418, 171–188.

Hart, S.R., Dunn, T., 1993. Experimental cpx/melt partitioning of 24 trace elements. Contrib. Mineral. Petrol. 113, 1–8.

Hellebrand, E., Snow, J.E., Dick, H.J.B., Hofmann, A., 2001. Coupled major and trace elements as indicators of the extent of melting in mid-ocean-ridge peridotites. Nature 410, 677–681.

Hirschmann, M.M., Tenner, T., Aubaud, C., Withers, A.C., 2009. Dehydration melting of nominally anhydrous mantle: the primacy of partitioning. Phys. Earth Planet. In. 176 (1–2), 54–68.

Ingrin, J., Skogby, H., 2000. Hydrogen in nominally anhydrous upper-mantle minerals: concentration levels and implications, 2000 Eur. J. Mineral 12, 543–570.

Ingrin, J., Latrous, K., Doukhan, J.C., Doukhan, N., 1989. Water in diopside: an electron microscopy and infrared spectroscopy study. Eur. J. Mineral 327–342.

Ionov, D.A., Bodinier, J.L., Mukasa, S.B., Zanetti, A., 2002. Mechanisms and sources of mantle metasomatism: major and trace element compositions of peridotite xenoliths from Spitsbergen in the context of Numerical Modelling. J. Petrol. 43, 2219–2259.

Jianping, L., Kornprobst, J., Vielzeuf, D., Fabries, J., 1995. An improved experimental calibration of the olivine-spinel geothermometer. Chin. J. Geochem. 14, 68–77.

Jochum, K.P., Stoll, B., Herwig, K., Willbold, M., Hofmann, A.W., Amini, M., Aarburg, S., Abouchami, W., Hellebrand, E., Mocek, B., Raczek, I., Stracke, A., Alard, O., Bouman, C., Becker, St, Dücking, M., Brätz, H., Klemd, R., de Bruin, D., Canil, D., Cornell, D., de Hoog, C.-J., Dalpé, C., Danyushevsky, L., Eisenhauer, A., Gao, Y., Snow, J.E., Groschopf, N., Günther, D., Latkoczy, C., Guillong, M., Hauri, E., Höfer, H.E., Lahaye, Y., Horz, K., Jacob, D.E., Kasemann, S.A., Kent, A.J.R., Ludwig, T., Zack, T., Mason, P.R.D., Meixner, A., Rosner, M., Misawa, K., Nash, B.P., Pfänder, J., Premo, W.R., Sun, W.D., Tiepolo, M., Vannucci, R., Vennemann, T., Wayne, D., Woodhead, J.D., 2006. MPI-DING reference glasses for in-situ microanalysis: new reference values for element concentrations and isotope ratios. G-cubed 7 (2), Q02008.

Jochum, K.P., Nohl, U., Herwig, K., Lammel, E., Stoll, B., Hofmann, A.W., 2005. GeoReM: Anew geochemical database for reference materials and isotopic standards. Geostand. Geoanal. Res. 29, 333–338.

Jochum, K.P., Weis, U., Stoll, B., Kuzmin, D., Yang, Q., Raczek, I., Jacob, D.E., Stracke, A., Birbaum, K., Frick, D.A., Günther, D., Enzweiler, J., 2011. Determination of reference values for NIST SRM 610-617 glasses following ISO Guidelines. Geostand. Geoanal. Res. 35 (4), 397–429.

Johnson, K.T.M., Dick, H.J.B., Shimizu, N., 1990. Melting in the oceanic upper mantle:an ion microprobe study of diopsides in abyssal peridotites. J. Geophys. Res. 95, 2661–2678.

Kemgang, Ghomsi, F.E., Sévérin, N., Mandal, A., Nyam, F.E.A., Tenzer, R., Tokam Kamga, A.P., Nouayou, R., 2020. Cameroon's crustal configuration from global gravity and topographic models and seismic data. J. Afr. Earth Sci. 103657.

Klemme, S., van der Laan, S.R., Foley, S.F., Gunther, D., 1995. Experimentally determined trace and minor element partitioning between clinopyroxene and carbonatite melt under upper mantle conditions. Earth Planet Sci. Lett. 133, 439–448.

Kovacs, I., Hermann, J., O'Neill, H. St C., FitzGerald, J.D., Sambridge, M., Horvath, G., 2008. Quantitative absorbance spectroscopy with unpolarized light, Part II: experimental evaluation and development of a protocol for quantitative analysis of mineral IR spectra. Am. Mineral. 93, 765–778.

Lee, D.C., Halliday, N., Davies, G.R., Essene, E.J., Fitton, G.J., Temdjim, R., 1996. Melt enrichment of shallow depleted mantle: a detailed petrological, trace element and isotopic study of mantle-derived xenoliths and megacrysts from the Cameroon Line. J. Petrol. 37, 415–441.

Lenoir, X., Garrido, C.J., Bodinier, J.L., Dautria, J.M., 2000. Contrasting lithospheric mantle domains beneath the Massif Central (France) revealed by geochemistry of peridotite xenoliths. Earth Planet Sci. Lett. 181, 359–375.

Li, P., Xia, Q.K., Deloule, E., Chen, H., Gu, X.Y., Feng, M., 2015. Temporal variation of H_2O content in the lithospheric mantle beneath the eastern North China craton: implications for the destruction of cratons. Gondwana Res. 28 (1), 276–287.

Li, Z.X., Lee, C.A., Peslier, A.H., Lenard, A., Mackwell, S.J., 2008. Water contents in mantle xenoliths from the Colorado Plateau and vicinity: implications for the mantle rheology and hydration-induced thinning of continental lithosphere. J. Geophys. Res. 113, B09210.

Liu, C.-Z., Yang, L.-Y., Li, X.-H., Tchoankoue, J.P., 2017. Age and Sr-Nd-Hf isotopes of the sub-continental lithospheric mantle beneath the Cameroon Volcanic Line: constraints from the Nyos mantle xenoliths. Chem. Geol. 455, 84–97.

Liu, J., Graham Pearson, D., Shu, Q., Sigurdsson, H., Thomassot, E., Alard, O., 2020. Dating post-Archean lithospheric mantle: insights from Re-Os and Lu-Hf isotopic systematics of the Cameroon Volcanic Line peridotites. Geochem. Cosmochim. Acta 278, 177–198.

Liu, S.A., Wang, Z.Z., Li, S.G., Huang, J., Yang, W., 2016. Zinc isotope evidence for a largescale carbonated mantle beneath eastern China. Earth Planet Sci. Lett. 444, 169–178.

Marzoli, A., Piccirillo, E.M., Renne, P.R., Bellieni, G., Iacumin, M., Nyobe, J.B., Aka, F.T., 2000. The Cameroon Volcanic Line revisited: petrogenesis of continental basaltic magmas from lithospheric and asthenospheric mantle sources. J. Petrol. 41, 87–109.

Marzoli, A., Aka, F.T., Merle, R., Callegaro, S., N'ni, J., 2015. Deep to shallow crustal differentiation of within-plate alkaline magmatism at Mt. Bambouto volcano, Cameroon Line. Lithos 220–223, 272–288.

Mbowou, G.I.B., Lagmet, C., Nomade, S., Ngounouno, I., Deruelle, B., Ohnenstetter, D., 2012. Petrology of the late Cretaceous peralkaline rhyolites (pantellerite and commendite) from lake Chad, central Africa. J. Geosci. 57, 127–141.

McCoy-West, A.J., Bennett, V.C., O'Neill, H.S.C., Hermann, J., Puchtel, I.S., 2015. The interplay between melting, refertilization and carbonatite metasomatism in off cratonic lithospheric mantle under Zealandia: an integrated major, trace and platinum group element study. J. Petrol. 56 (3), 563–604.

McDonough, W.F., Sun, S.-s., 1995. The composition of the Earth. Chem. Geol. 120, 223–253.

Mercier, J.-C.C., Carter, N.L., 1975. Pyroxene geotherms. J. Geophys. Res. 80, 3349–3362.

Moundi, A., Ménard, J.-J., Reusser, E., Tchoua, M.F., Dietrich, V.J., 1996. Découverte de basaltes transitionnels dans le secteur continental de la Ligne du Cameroun (massif du Mbam, Ouest-Cameroun): Compt. Rendus Académ. Sci. de Paris 322, 831–837.

Moundi, A., Wandji, P., Bardintzeff, J.-M., Ménard, J.-J., Okomo Atouba, L.C., Reusser, E., Bellon, H., Tchoua, M.F., 2007. Les basaltes éocènes à affinité transitionnelle du plateau Bamoun, témoins d'un réservoir mantellique enrichi sous la ligne volcanique du Cameroun. Compt. Rendus Geosci. 339, 396–406.

Ngounouno, I., Nguihdama, D., Kamgang, P., Deruelle, B., 2008. Petrology of spinel lherzolite xenoliths in alkali basalts from Liri, south of the Kapsiki plateau (northernmost Cameroon hot line). J. Cameroon Acad. Sci. 8 (1), 31–42.

Ngounouno, I., Déruelle, B., Demaiffe, D., 2000. Petrology of the Bimodal Cenozoic volcanism of the Kapsiki plateau (northernmost Cameroon, central Africa). J. Geothermal Res 102, 21–44.

Norman, M.D., 1998. Melting and metasomatism in the continental lithosphere: laser ablation ICPMS analysis of minerals in spinel lherzolites from eastern Australia Contrib. Mineral. Petrol. 130, 240–255, 1998.

O'Leary, J.A., Gaetani, G.A., Hauri, E., 2010. The effect of tetrahedral Al^{3+} on the partitioning of water between clinopyroxene and silicate melt. Earth Planet Sci. Lett. 297, 111–120.

O'Reilly, S.Y., Griffin, W.L., 1988. Mantle metasomatism beneath western Victoria, Australia: I. Metasomatic processes in Cr-diopside lherzolites. Geochem. Cosmochim. Acta 52, 433–447, 1988.

Palme, H., O'Neill, H.S.C., 2014. Cosmochemical estimates of mantle composition. Treatise Geochem. 1–39.

Pasyanos, M., Nyblade, A., 2007. A top to bottom lithospheric study of Africa and Arabia. Tectonophysics 444 (1–4), 27–44.

Patkó, L., Liptai, N., Kovács, I.J., Aradi, L.E., Xia, Q.-K., Ingrin, J., Mihály, J., O'Reilly, S., Griffin, W.L., Wesztergom, V., Szabó, C., 2019. Extremely low structural hydroxyl contents in upper mantle xenoliths from the Nógrád-Gömör Volcanic Field (northern Pannonian Basin): geodynamic implications and the role of post-eruptive reequilibration. Chem. Geol. 507, 23–41.

Paton, C., Hellestrom, J., Paul, B., Woodhead, J., Hergt, J., 2011. Iolite: freeware for the visualisation and processing of mass spectrometric data. J. Anal. At. Spectrom. 26, 2508–2518.

Pearce, J.A., Barker, P.F., Edwards, S.J., Parkinson, I.J., Leat, P.T., 2000. Geochemistry and tectonic significance of peridotites from the South Sandwich arc-basin system, South Atlantic. Contrib. Mineral. Petrol. 139 (1), 36–53.

Pearce, J.A., Stern, R.J., Bloomer, S.H., Fryer, P., 2005. Geochemical mapping of the Mariana arc-basin system: implications for the nature and distribution of subduction components. G-cubed 6, Q07006.

Pearson, D.G., Canil, D., Shirey, S.B., 2014. Mantle samples included in volcanic rocks. Treatise Geochem. 169–253.

Peslier, A.H., Luhr, J.F., Post, J., 2002. Low water contents in pyroxenes from spinel-peridotites of the oxidized, sub-arc mantle wedge. Earth Planet Sci. Lett. 201 (1), 69–86.

Peslier, A.H., Luhr, J.F., 2006. Hydrogen loss from olivines in mantle xenoliths from Simcoe (USA) and Mexico: mafic alkalic magma ascent rates and water budget of the subcontinental lithosphere. Earth Planet Sci. Lett. 242 (3–4), 302–319.

Peslier, A.H., Woodland, A.B., Bell, D.R., Lazarov, M., Lapen, T.J., 2012. Metasomatic control of water contents in the Kaapvaal cratonic mantle. Geochem. Cosmochim. Acta 97, 213–246.

Pintér, Zs, Patkó, L., Djoukam, J.F.T., Kovács, I., Tchouankoue, J.P., Falus, G., Konc, Z., Tommasi, A., Barou, F., Mihály, J., Németh, Cs, Jeffries, T., 2015. Characterization of the sub-continental lithospheric mantle beneath the Cameroon volcanic line inferred from alkaline basalt hosted peridotite xenoliths from Barombi Mbo and Nyos Lakes. J. Afr. Earth Sci. 111, 170–193.

Poudjom-Djomani, Y.H., Nnange, J.M., Diament, M., Ebinger, C.J., Fairhead, J.D., 1995. Effective elastic thickness and crustal thickness variations in West Central Africa inferred from gravity data. J. Geophys. Res. Solid Earth 100 (10–11), 22047–22070.

Prechtel, F., Stalder, R., 2012. OH-defects in Al- and Cr- doped synthetic enstatites and defect geobarometry on natural orthopyroxenes from Earth's mantle. Eur. J. Mineral 24, 471–481.

Regnoult, J.M., 1986. Cameroon Geological Synthesis. Department of Mines and Geology, Yaounde, p. 119p.

Rudnick, R.L., McDonough, W.F., Chappell, B.W., 1993. Carbonatite metasomatism in the northern Tanzanian mantle: petrographic and geochemical characteristics. Earth Planet Sci. Lett. 114, 463–475.

Schmädicke, E., Gose, J., Will, T.M., 2011. Heterogeneous mantle underneath the North Atlantic: evidence from water in orthopyroxene, mineral composition and equilibrium conditions of spinel peridotite from different locations at the Mid-Atlantic Ridge. Lithos 125, 308–320.

Scott, J.M., Liu, J., Pearson, D.G., Waight, T.E., 2016. Mantle depletion and metasomatism recorded in orthopyroxene in highly depleted peridotites. Chem. Geol. 441, 280–291.

Scott, J.M., Waight, T.E., van der Meer, Q.H.A., Palin, J.M., Cooper, A.F., Münker, C., 2014a. Metasomatized ancient lithospheric mantle beneath the young Zealandia microcontinent and its role in HIMU-like intraplate magmatism. G-cubed 15 (9), 3477–3501.

Scott, J.M., Hodgkinson, A., Palin, J.M., Waight, T.E., Van der Meer, Q.H.A., Cooper, A. F., 2014b. Ancient melt depletion overprinted by young carbonatitic metasomatism in the New Zealand lithospheric mantle. Contrib. Mineral. Petrol. 167, 963.

Shaw, C.S.J., Dingwell, D.B., 2008. Experimental peridotite–melt reaction at one atmosphere: a textural and chemical study. Contrib. Mineral. Petrol. 155, 199–214.

Shaw, C.S.J., Heidelbach, F., Dingwell, D.B., 2006. The origin of reaction textures in mantle peridotite xenoliths from Sal Island, Cape Verde: the case for "metasomatism'' by the host lava. Contrib. Mineral. Petrol. 151, 681–697.

Shu, Q., Brey, G.P., 2015. Ancient mantle metasomatism recorded in subcalcic garnet xenocrysts: temporal links between mantle metasomatism diamond growth and crustal tectono magmatism Earth Planet. Sci. Lett. 418, 27–39.

Skogby, H., Bell, D.R., Rossman, G.R., 1990. Hydroxide in pyroxene; variations in the natural environment. Am. Mineral. 75 (7–8), 764–774.

Stalder, R., Ludwig, T., 2007. OH incorporation in synthetic diopside, 2007 Eur. J. Mineral 19 (3), 373–380.

Streckeisen, A., 1976. To each plutonic rock its proper name. Earth Sci. Rev. 12 (1), 1–33, 1976.

Su, B.-X., Zhang, H.-F., Sakyi, P.A., Ying, J.-F., Tang, Y.-J., Yang, Y.-H., Zhao, X.-M., 2010. Compositionally stratified lithosphere and carbonatite metasomatism recorded in mantle xenoliths from the Western Qinling (Central China). Lithos 116 (1–2), 111–128.

Su, B.X., Zhang, H.F., Sakyi, P.A., Zhang, Y.H., Ying, J.F., Tang, Y.J., Qin, K.Z., Xiao, Y., Zhao, X.M., Mao, Q., Ma, Y.G., 2011. The origin of spongy texture in minerals of mantle xenoliths from the Western Qinling, central China. Contrib. Mineral. Petrol. 161, 465–482.

Tamen, J., Nkoumbou, C., Reusser, E., Tchoua, F., 2015. Petrology and geochemistry of mantle xenoliths from the Kapsiki plateau (Cameroon volcanic line): implications for lithospheric upwelling. J. Afr. Earth Sci. 101, 119–134.

Tedonkenfack, S.S.T., Puziewicz, J., Aulbach, S., Ntaflos, T., Kaczmarek, M.-A., Matusiak-Małek, M., Kukuła, A., Ziobro, M., 2021. Lithospheric mantle refertilization by DMM-Derived melts beneath the Cameroon Volcanic Line – a case study of the Befang xenolith suite (Oku Volcanic Group, Cameroon). Contrib. Mineral. Petrol. 176, 37.

Teitchou, M.I., Grégoire, M., Temdjim, R., Ghogomu, R.T., Ngwa, C., Aka, F.T., 2011. Mineralogical and geochemical fingerprints of mantle metasomatism beneath Nyos volcano (Cameroon volcanic line). In: Beccaluva, L., Bianchini, G., Wilson, M. (Eds.), Volcanism and Evolution of the African Lithosphere: Geological Society of America Special Paper 478, pp. 193–210.

Tian, Z.Z., Liu, J., Xia, Q.K., Ingrin, J., Hao, Y.T., Depecker, C., 2017. Water concentration profiles in natural mantle orthopyroxenes: a geochronometer for long annealing of xenoliths within magma. Geology 45 (1), 87–90.

Tokam, A.-P.K., Tabod, C.T., Nyblade, A.A., Julià, J., Wiens, D.A., Pasyanos, M.E., 2010. Structure of the crust beneath Cameroon, West Africa, from the joint inversion of Rayleigh wave group velocities and receiver functions. Geophys. J. Int. 183, 1061–1076.

Tollan, P.M.E., Hermann, J., 2019. Arc magmas oxidized by water dissociation and hydrogen incorporation in orthopyroxene. Nat. Geosci. 12 (8), 667–671.

Tollan, P.M.E., O'Neill, H.StC., Hermann, J., Benedictus, A., Arculus, R.J., 2015. Frozen melt-rock reaction in a peridotite xenolith from sub-arc mantle recorded by diffusion of trace elements and water in olivine. Earth Planet Sci. Lett. 422, 169–181.

Tollan, P.M.E., O'Neill, H.S.C., Hermann, J., 2018. The role of trace elements in controlling H incorporation in San Carlos olivine. Contrib. Mineral. Petrol. 173 (11).

Tollan, P.M.E., Smith, R., O'Neill, H.S.C., Hermann, J., 2017. The responses of the four main substitution mechanisms of H in olivine to H_2O activity at 1050 °C and 3 GPa. Prog. Earth Planet. Sci. 4 (1).

Toteu, S.F., Van Schmus, W.R., Penaye, J., Michard, A., 2001. New U-Pb, and Sm-Nd data from North-Central Cameroon and its bearing on the pre-Pan-African history of Central Africa. Pre. Res. 108, 45–73.

Toteu, S.F., Penaye, J., Djomani, Y.P., 2004. U–Pb and Sm-Nd evidence for Eburnean and PanAfrican high-grade metamorphism in cratonic rocks of southern Cameroon. Can. J. Earth Sci. 41, 73–85.

Tsozué, D., Nzeugang, A.N., Azinwi, P.T., 2017. Genesis and classification of Soils developed on Gabbro in the high Reliefs of Maroua region, North Cameroon. Eurasian J. Soil Sci. 6, 168–177.

Uenver-Thiele, L., Woodland, A.B., Seitz, H.-M., Downes, H., Altherr, R., 2017. Metasomatic processes revealed by trace element and redox signatures of the lithospheric mantle beneath the massif central, France. J. Petrol. 58 (3), 395–422.

Van der Lee, S., Regenauer-Lieb, K., Yuen, D.A., 2008. The role of water in connecting past and future episodes of subduction. Earth Planet Sci. Lett. 273, 15–27.

Vincent, P.M., Armstrong, R.L., 1973. Volcanism of the Kapsiki Plateau (North Cameroon) and the Underlying Sedimentary Formations. Coll. African Geol., Florence, abst. unpubl.

Walter, M.J., 2003. Melt extraction and compositional variability in mantle lithosphere. In: Holland, H.D., Turekian, K.K. (Eds.), Treatise on Geochemistry. Elsevier, pp. 363–394.

Wang, C., Jin, Z.M., Gao, S., Zhang, J.F., Zheng, S., 2010. Eclogite-melt/peridotite reaction: experimental constraints on the destruction mechanism of the North China Craton. Sci. China Earth Sci. 40, 541–555.

Warren, J.M., 2016. Global variations in abyssal peridotite compositions. Lithos 248–251, 193–219.

Witt-Eickschen, G., O'Neill, H.S.C., 2005. The effect of temperature on the equilibrium distribution of trace elements between clinopyroxene, orthopyroxene, olivine and spinel in upper mantle peridotite. Chem. Geol. 221 (1–2), 65–101.

Workman, R.K., Hart, S.R., 2005. Major and trace element composition of the depleted MORB mantle (DMM). Earth Planet Sci. Lett. 231, 53–72.

Xia, Q.K., Hao, Y.T., Li, P., Deloule, E., Coltorti, M., Dallai, L., Yang, X.Z., Feng, M., 2010. Low water content of the Cenozoic lithospheric mantle beneath the eastern part of the North China Craton. J. Geophys. Res. Solid Earth 115, B07207.

Xu, Y.-G., Menzies, M.A., Thirlwall, M.F., Huang, X.-L., Liu, Y., Chen, X.-M., 2003. "Reactive" harzburgites from Huinan, NE China: products of the lithosphereasthenosphere interaction during lithospheric thinning? Geochem. Cosmochim. Acta 67 (3), 487–505.

Yaxley, G.M., Green, D.H., 1998. Reactions between eclogite and peridotite: mantle refertilisation by subduction of oceanic crust. Schweiz. Miner. Petrogr. Mitt. 78, 243–255.

Yaxley, G.M., Green, D.H., Kamenetsky, V., 1998. Carbonatite metasomatism in the Southeastern Australian lithosphere, 1917–1930 J. Petrol. 39 (11–12).

Zangana, N., Downes, H., Thirlwall, M., Marriner, G., Bea, F., 1999. Geochemical variation in peridotite xenoliths and their constituent clinopyroxenes from Ray Pic (French Massif Central): implications for the composition of the shallow lithospheric mantle. Chem. Geol. 153 (1–4), 11–35.

Zong, K., Liu, Y., 2018. Carbonate metasomatism in the lithospheric mantle: implications for cratonic destruction in North China. Sci. China Earth Sci. 61, 711–729.

Further reading

Matsukage, K.N., Oya, M., 2010. Petrological and chemical variability of peridotite xenoliths from the Cameroon Volcanic Line, West Africa: an evidence for plume emplacement. J. Mineral. Petrol. Sci. 105, 57–69.

Njombie Wagsong, P.M., Temdjim, R., Foley, S.F., 2018. Petrology of spinel lherzolitexenoliths from Youkou volcano, Adamawa Massif, Cameroon Volcanic Line: mineralogical and geochemical fingerprints of sub-rift mantle processes. Contrib. Mineral. Petrol. 173, 13.

Nkouandou, O.F., Bardintzeff, J.-M., Fagny, A.M., 2015. Sub-continental lithospheric mantle structure beneath the Adamawa plateau inferred from the petrology of ultramafic xenoliths from Ngaoundéré (Adamawa plateau, Cameroon, Central Africa). J. Afr. Earth Sci. 111, 26–40.

Temdjim, R., Njombie Wagsong, P.M., Nzakou, T.J.A., Foley, S.F., 2019. Variation in mantle lithology and composition beneath the Ngao Bilta volcano, AdamawaMassif, Cameroon volcanic line, West-central Africa. Geosci. Front. 11, 665–677.